4-2013

Nanocluster Production for Solar Cell Applications

Haila M Aldosari

Follow this and additional works at: https://scholarworks.uaeu.ac.ae/all_theses

  Part of the Materials Science and Engineering Commons

Recommended Citation

United Arab Emirates University

College of Engineering

Material Science and Engineering Graduate Program

NANOCLUSTER PRODUCTION FOR SOLAR CELL APPLICATIONS

By

Haila M. Aldosari

Thesis is submitted in partial fulfillment of the requirements for the Master of Material Science and Engineering degree

Under the direction of Dr. Ahmad Ayesh

April, 2013

I, Haila Mohammed Aldosari, the undersigned, a graduate student at the United Arab Emirates University (UAEU) and the author of the thesis titled "NANOCLUSTER PRODUCTION FOR SOLAR CELL APPLICATIONS", hereby solemnly declare that this thesis is an original work done and prepared by me under the guidance of Prof. Ahmed Ayesh, in the college of science at UAEU. This work has not been previously formed as the basis for the award of any degree, diploma or similar title at this or any other university. The materials borrowed from other sources and included in my thesis have been properly acknowledged.

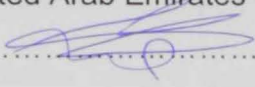Student's Signature ....Haila............   Date ...4/6/2013

Approved by

Advisory Committee

Advisor: Dr. Ahmad I. Ayesh

Title: Assistant Professor of Physics

Department: Department of Physics

Institution: United Arab Emirates University

Signature: .... Date ...27/5/2013

Internal Examiner: Prof. Yousef Haik

Title: Professor

Department: Department of Mechanical Engineering

Institution United Arab Emirates University

Signature .... Date ....

External Examiner: Dr. Dagou Zeze

Title: Senior Lecturer in Nanotchnology & Microsystems

Department: School of Engineering & Computer Science

Institution: Durham University

Signature .... Date ....

Master's Program Coordinator Dr. Saud Aldajah

Department: Department of Mechanical Engineering

Institution: United Arab Emirates University

Signature .... Date ....

Associate Dean for Research & Graduate Studies: Dr. Ali Al-Marzouqi

Signature .... Date ....

iv

ABSTRACT

This research focuses on the fabrication and characterization of silicon (Si) and silver (Ag) nanoclusters that might be used for solar cell applications. Silicon and silver nanoclusters have been synthesized by means of inert gas condensation method and dc magnetron sputtering source inside an ultra-high vacuum system. The nanocluster source produces ionized nanoclusters that enable the study of the nanocluster size distribution using a quadrupole mass filter (QMF). We have found that nanocluster size distribution can be tuned by various source parameters, such as the sputtering discharge power (P), argon inert gas flow rate (f_{Ar}), and aggregation length (L).

Transmission electron microscopy (TEM) have been done to evaluate the size distribution of Si and Ag nanoclusters and to confirm the measurements performed using the quadrupole mass filter results. The Si nanocluster size distributions were controlled to change in the range of 3.33 ± 0.27 to 7.36 ± 0.52 nm by controlling the source conditions. On the other hand, Ag nanoclusters with average size in the range of 3.65 ± 0.05nm to 8.25 ± 0.15 nm were synthesized by altering the source conditions. This work illustrates the ability of controlling the Si and Ag nanoclusters' size by proper optimization of the operation conditions. By controlling the Si and Ag nanoclusters size, one can alter their surface properties to suit our needs to enhance the solar cell efficiency. The current work also discusses the nanocluster formation mechanisms. Herein, Ag nanoclusters were deposited on commercial polycrystalline solar cells. Short circuit current (I_{SC}), open circuit voltage (V_{OC}), fill factor (FF), and efficiency (η) were obtained under light source with an intensity of 30 mW/cm^2. A 22.7% enhancement in solar cell efficiency could be measured after deposition of Ag nanoclusters which

demonstrates that Ag nanoclusters generated in this work are useful to enhance solar cell efficiency. The research has underlined promising results and many other ideas that can be implemented in the future for solar cell applications.

ACKNOWLEDGEMENTS

DEDICATION

This thesis is dedicated to my Mother.

TABLE OF CONTENTS

LIST OF TABLES

LIST OF FIGURES

LIST OF ACRONYMS AND ABBREVIATIONS

AFM	Atomic force microscopy
cm	Centimeter
D	Diameter
f_{Ar}	Argon flow rate
FF	Fill factor
IGC	Inert gas condensation
I_{SC}	Short-circuit current
J_{SC}	Short-circuit current density
L	Agreggation length
m	Meter
MFC	Mass flow controller
mm	Millimetre
µm	Micrometer
nm	Nanometer
P	Power
PLS	Photoluminescence spectroscopy
PVD	Physical vapor deposition
QCM	Quartz crystal monitor
QMF	Quadrupole mass filter
SEM	Scanning electron microscopy
SOI	silicon-on-insulator
SPB	Surface plasmon band
SPR	Surface plasmon resonance
TEM	Transmission electron microscope
TOF	Time of flight
V_{OC}	Open-circuit voltage
XRD	X-ray diffraction
η	efficiency
λ	Wavelength

CHAPTER ONE: AN OVERVIEW

1.1 What is nanotechnology?

The term nanotechnology was first used in 1974 by Norio Taniguchi (University of Tokyo) to refer the ability to design, characterize, produce and build materials precisely at nanometer scale that can be used to make complete, high performance products [1-2].Nanotechnology is thus defined as a generic term for applications that work with matter at nanometer scale dimensions. At this size scale, the material's physical, chemical and biological properties are different from what they were in their bulk form. Nano-scale materials exhibit unique and superior properties that are not found in bulk materials. Their uniqueness arises from two main reasons. First, the quantum confinement effects of their electrons [3]. Second, as particles get smaller; their surface area to volume ratio increase dramatically such that the nano-scale materials have higher surface to volume ratios compared to the same amount of bulk material. What is so interesting about increase surface area to volume ratio is that, reactions take place at the surface of a chemical or material; the greater the surface for the same volume, the greater the reactivity. Therefore, as a nanocluster getting smaller, the percentage of atoms on the surface of a nanocluster is getting higher compared to bulk material implying more atoms exposed to the reaction which will affect their strength or electrical properties [4]. Thus, in some cases materials that are inert in their larger form are reactive when produced in their nanoscale form.

A main objective of researchers in nanotechnology is to study variation in nanoclusters' properties as their sizes increase from atoms or molecules in order to understand the evolution of the physical and chemical properties with the growth of the materials due to the quantum confinement effect and compare those properties with the corresponding bulk properties. By harnessing these new properties, researchers have found that they can develop materials, devices and systems that are superior to be used for many applications today. Hence, size control of the material is the essence of nanotechnology. In addition, nano-scale materials exhibit superior thermal stability, mechanical strength, catalytic activity, electrical conductivity, magnetic and optical properties. Therefore, nanotechnology penetrates all areas of physical, chemical and biological sciences and applications as well as other interdisciplinary fields. This made nano-scale materials the subject of active research for various applications such as solar cells [5], optoelectronic device[6], catalysis[7], carrier systems for drug delivery [8], cancer treatment [9] …etc.

1.2 How small is the nano?

The prefix of "nano" was driven from the Greek word for "dwarf". A nanometer is a one millionth of a millimeter, or to put it comparatively, is the characteristic scale of molecules (groups of atoms bound covalently together). Each atom is of the order of 1Å in size (0.1 nm): hence a nano-object may contain tens to millions of atoms to achieve the nano- size [4]. To get a feel of the smallness of the nanometer, we note that 1nm about

2

1/80,000 of the diameter of a human hair. To get a perspective of the scale

of a nanometer, Fig. 1 shows a sequence of images of objects of different

sizes.
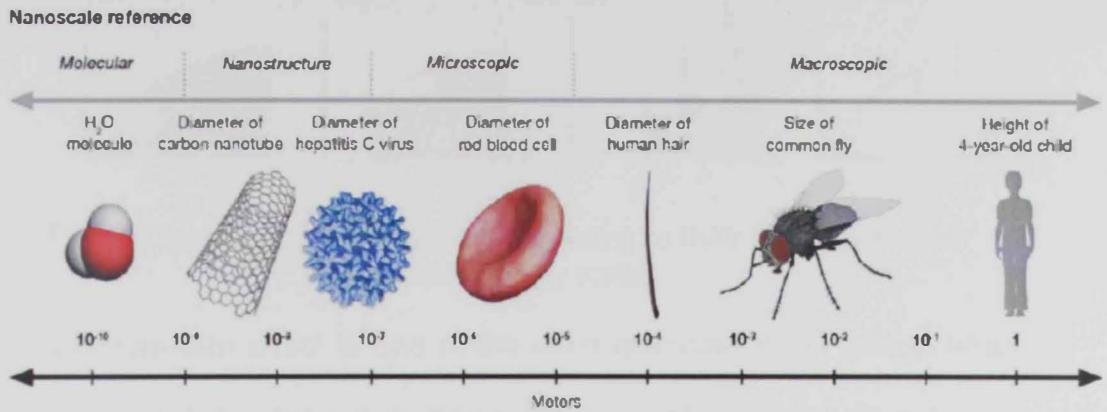
Fig. 1. Sequence of images showing the various levels of scale [10].

1.3 What is happening in the Nano-scale?

1.3.1 Quantum confinement effect

Approaching the nano-size range of a material size will reduce the

effective dimensionality of the region that constrains the electron's wave

function, from a 3D bulk solid, to a 2D quantum well, to a 1D quantum

wire, and finally to a 0D quantum dot (nanocluster), as illustrated in Fig.

2.Therefroe, the electron density will change accordingly.
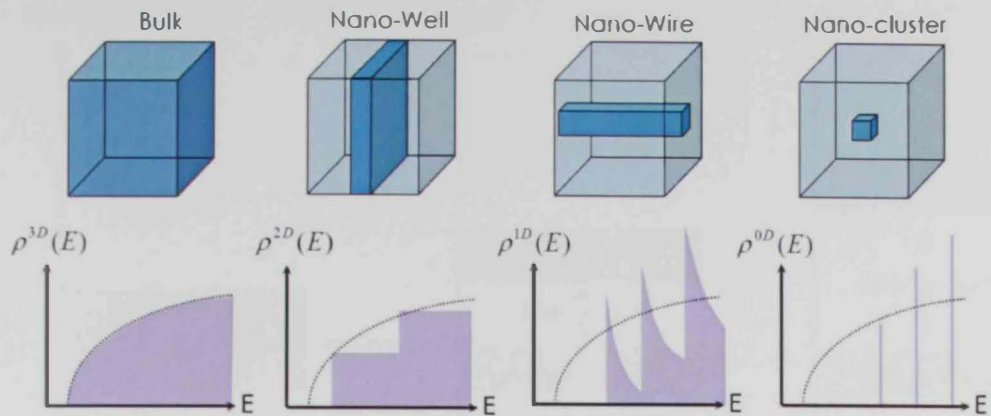
Fig. 2. Classification of materials according to their dimensions and electron density states.

Quantum size effect is one of the most observed direct effects when approaching the nano-scale range of the material size, due to the confinement of the electrons affecting the optical, electrical and magnetic behavior of materials [3, 4]. By quantum mechanics, any object that is confined within a boundary has specific allowed energy levels and other forbidden ones. In bulk materials, the presence of many atoms causes splitting of the electronic energy levels, giving continuous energy bands separated by a forbidden band. The lower-energy band, mostly filled band, is called the valence band and the next higher available energy band, mostly empty band, is called the conduction band. The difference in energy between the valence band and the conduction band is called an energy gap and it is fixed for a given material. No free electron present in the forbidden energy gap. Figure 3 illustrates the energy band diagram for different types of material [11]. The figure shows that the energy bands of conductors overlap, whereas the conduction band and valence bands are separated by a relatively narrow energy gap for semiconductors and relatively wider energy gap for insulators.
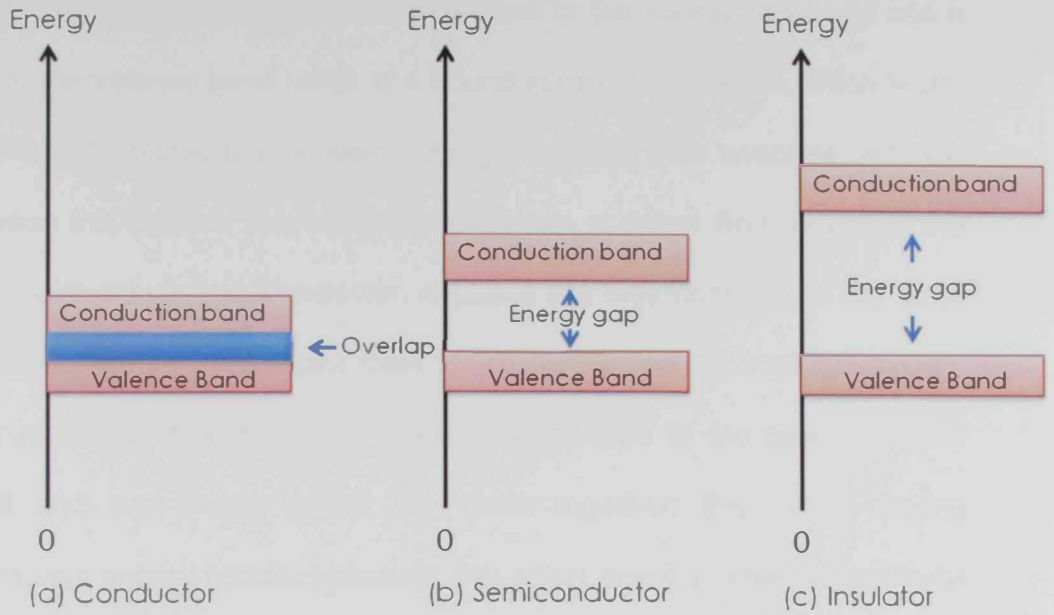
Fig. 3. Energy bands for (a) conductors, (b) semiconductors, and (c)
Insulators. (Adapted from reference [11])

In semiconducting materials, valence electrons can absorb some sort
of stimulus such as light or thermal excitation and getting excited across
the energy gap, gaining enough energy to jump cross the energy gap and
move into the conduction band, leaving a positive (hole) behind at the
valence band as illustrated in Fig. 4 [11].
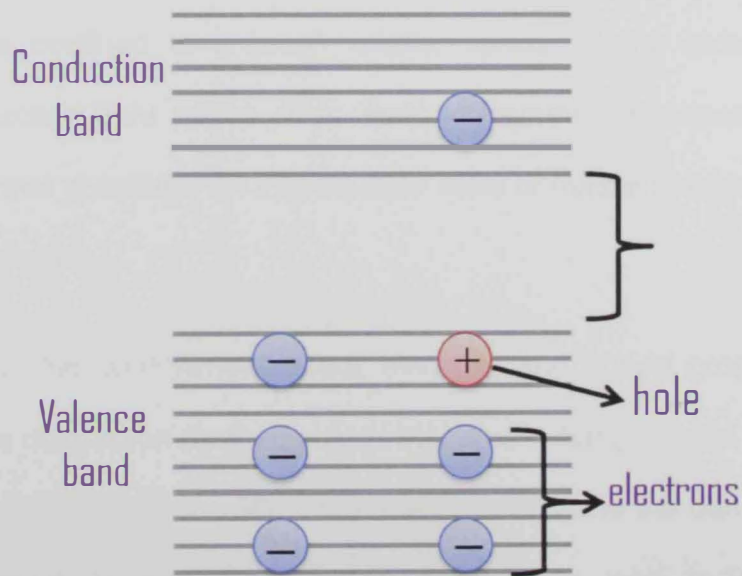
Fig. 4 Electron excitation from the valence band to conduction band [11].

The interaction between an electron in the conduction band and a hole in the valence band leads to a bound state called exciton which is due to Coulomb interaction between charge carriers. The average distance between the electron and corresponding hole is called Bohr radius of the exciton. In a bulk semiconductor, excitons are only confined to the large volume of the semiconductor itself which is much larger than the exciton Bohr radius, so the minimum allowed energy level of the exciton is very small and the energy levels are close together; this helps making continuous energy bands. However, this effect develop when the material dimensions shrink and approach the de Broglie wavelength of the electron in a quantum well structure and when the radius of a semiconductor sphere is smaller than the bulk Bohr radius of the exciton, in a nanoclusters. This introduce dramatic changes in the energy bands, as the continuous density of states in bulk is replaced with a set of discrete energy levels that are directly related to their size. In nanoclusters, relatively few atoms are present which cuts down the splitting, and the excitons are confined to a much smaller space, of the order of the material's exciton Bohr radius. This leads to discrete, quantized, energy levels such that constitute an intermediate state of matter between atoms and bulk materials.

Due to the confinement effect, electrical and optical properties of nanoclusters depend on their size such that small change to the size and composition of nanoclusters allow the energy levels, and the band gap, to be manipulated to specific energies which may lead to changing nanoclusters' electrical and optical sharply. In other word, changing their

size or composition allow scientists to tune their optical properties such that they can fluoresce different colors using a single light source. This effect was first observed in 1926 for CdS colloids [12]. Scientists have studied nanostructures extensively in the past two decades in order to understand the quantum size effect for various semiconducting and metal nanoclusters. The ability of controlling the band gap of nanoclusters allows the construction of high efficiency solar cells by utilizing much more of the sun's spectrum than before.

Nanoclusters are nearly zero-dimensional where in such system the excitons are confined in all three directions (the motion of electrons is restricted), which can be modeled using a particle in a box. The electron and the hole can be seen as hydrogen in the Bohr model with the hydrogen nucleus replaced by the hole of positive charge and negative electron mass.

Due to the confinement effect the energy gap increases compared to bulk material. Taking both electrons and holes into account the increase in gap energy is given by

$$\Delta E_g = \frac{\hbar^2}{2\mu} \left(\frac{\pi}{a}\right)^2 n^2 \quad (1\text{-}1)$$

Where $\frac{1}{\mu} = \frac{1}{m_e} + \frac{1}{m_p}$ is the reduced mass.

The above equation implies that as the size of the nanocluster decreases, the band gap between the filled valence band levels and the empty conduction band levels increases. Hence, by changing the size of

the nanocluster, the confinement of the energy of the exciton can be controlled.

1.3.2 Surface area to volume ratio

The surface area to volume ratio in a nanocluster has a significant effect on the nanoclusters chemical properties. Nanoclusters have relatively larger surface area to volume when compared to its equivalent bulk material. For example, the surface area to volume ratio of a sphere is $3/r$, where r is the radius of the sphere. As the radius of a sphere decreases its surface area to volume ratio increases and vice versa. For example, if a cube is divided into smaller piece, the surface area to volume of each smaller cube increases. For a block of material with 1m each side, as shown in Fig. 5, the surface area of this block is 6 m^2 and the volume is 1 m^3.

Area= $6 \times 1m^2 = 6m^2$ Area= $6 \times (1/2m)^2 \times 8 = 12m^2$
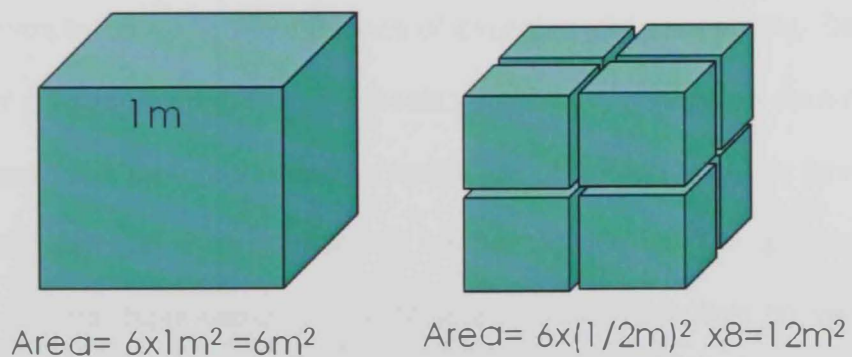
Fig. 5. Schematics drawing showing that the total surface area increases as one cut the block into smaller pieces, but the total volume remains constant.

Thus, the surface area to volume ratio for the block is 6. If one cut the block into 8 pieces that are one-half of a meter per side, the surface area to volume ratio will be doubled. Hence, nanoclusters have a much greater surface area per unit volume compared with the equivalent larger particles. Consequently, nanoclusters are more chemically reactive than the same amount of bulk material. More surface area means more places for light and chemicals to bind or react with a nanocluster. The large surface area to volume ratio of nanoclusters opens many possibilities for creating new materials that are highly reactive for different applications.

1.4 The work objectives

The objectives of this project are the fabrication of silicon (Si) and silver (Ag) nanoclusters by means of inert gas condensation method and to control and optimize the nanocluster size and the number of produced nanoclusters by studying the influence of experimental parameters. Silicon and silver nanoclusters will be synthesis using a dc magnetron sputtering source and inert gas condensation inside an ultra-high vacuum system. The nanoclusters' size distribution will be investigated using a quadrupole mass filter. The dependence of nanoclusters' size distribution on various source parameters, such as the sputtering discharge power, aggregation length, and inert gas flow rate will be examined. The morphology and structure of the produced nanoclusters will be investigated by transmission electron microscopy (TEM).Additionally, the produced Ag nanoclusters will

be deposited on a commercial solar cell and its electrical characteristics will be investigated.

Chapter Two: Literature Review

2.1 Introduction

In the recent years, there has been a growing interest in the fabrication and characterization of nanoclusters and rigorous effort has been directed towards utilizing them for industrial applications. Nanoclusters exhibit different properties (mechanical, optical, electrical, magnetic, chemical and electronic) which are not found in their corresponding bulk systems, which make them suitable for new applications.

Nanoclusters can be used for biosensors, nanofabricated medical devices [14] and even in immobilize proteins [15] due to their enhanced properties and size which is in the size range of important biological molecules such as DNA and proteins, etc. Also, nanoclusters are mainly used in semiconductor industry by controlling their size to enhance the efficiency of photovoltaic materials, and to fabricate microelectronic devices such as memories, processers and transistors [16].

Nanoclusters are divided into several categories depending on the type of these nanoclusters such as metallic, non-metallic, semiconductor and organic nanoclusters, which have immense surface area to volume ratio and quantum-size effect. Metal and semiconductor nanoclusters possess unique optical properties and are promising candidates for variety of applications in nanotechnology [3, 17].

2.2 Why silicon and silver nanoclusters?

Special attention has been paid on the synthesis of silicon nanoclusters due to their broad range of emerging and exciting applications in advance technologies such as computer chips, high-density information storage and photovoltaic cells [18]. Silicon is the principal component of most semiconducting devices and has a wide scope of applications because it remains a semiconductor at higher temperatures which is different than the germanium semiconductor, in addition to its low cost [19, 20]. Therefore, the synthesis of semiconducting nanoclusters such Si has significant implications for the fabrication of devices such as nanocluster based photovoltaic and light emitting devices [21]. Researchers reported that utilization of silicon nanoclusters into a silicon solar cell can increase the power efficiency, reduce heat generated and extend the cell's life time [18]. Without silicon nanoclusters, normal solar cells typically function in the visible light spectrum only. Whereas, ultraviolet light is either filtered out or absorbed by silicon and causes heat damage instead of the desired electrical current. Thus, fabrication a solar cell from silicon nanoclusters of the desired size may enhance the efficiency of the solar cell, by providing the ability to utilize ultraviolet light. At the nanoscale the indirect nature of Si energy gap is replaced by a strong direct energy gap [18]. By using Si nanoclusters in solar cells, the recombination of excitons is decreasing as a result of the strong confinement of conduction electrons. Thin-film of Si solar cells exhibit significantly low cost for producing photovoltaics. Light trapping is

particularly critical in such thin-film crystalline silicon solar cells in order to increase light absorption and hence cell efficiency.

On the other hand, silver nanoclusters have unique novel optical, thermal and electrical properties that can be used in numerous applications that take advantage of their unique properties that range from photovoltaics to biological and chemical sensors due to their high electrical conductivity, stability and low sintering temperatures.

Silver nanoclusters show beautiful novel colors, can be found in stained glass windows, received considerable attention from researchers. Silver nanoclusters are remarkably efficient at scattering and absorbing light and have a color that depends on the size and shape of the nanoclusters, interparticle interactions, dielectric properties, and local environment of the nanocluster [18]. Taking the above advantages of silver nanoclusters, plasmonic excitation using silver nanoclusters is developed to enhance the light absorption inside the photovoltaic material, thus solar cell efficiency. A plasmon can be due to the strong interaction of the silver nanoclusters with light [22]. Conduction electrons on the metal surface undergo a collective oscillation when excited by light at particular wavelengths. This electron oscillation around the particle surface causes a charge separation with respect to the ionic lattice, forming a dipole oscillation along the direction of the electric field of the light as illustrated in Fig. 6 [23, 24].

13
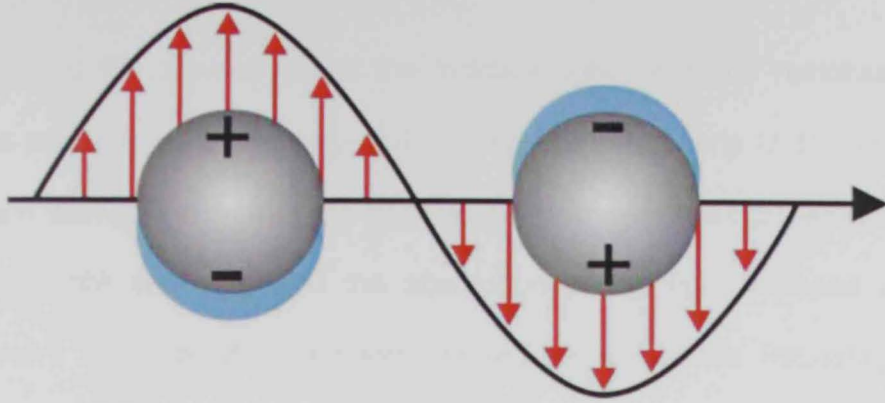
Fig. 6. Schematic illustration of surface plasmon resonance in plasmonic nanoclusters [25].

The movement of these electrons acts as a restoring force, allowing resonance to take place at a specific frequency, which is called the dipole surface plasmon resonance frequency (ω) [23 - 26]. This interaction is termed as surface plasmon resonance (SPR). SPR induces a strong absorption of the incident light depending on the nanocluster size. Mie's theory have described the extinction of light (the sum of absorption and scattering) of spherical particles of different sizes which known as the surface plasmon band (SPB) by solving Maxwell equations [27]. In order to understand this, one needs to evaluate all mentioned parameters and especially the dielectric properties. According to Mie's theory the particle and the surrounding medium are homogeneous, hence can be describe by bulk dielectric functions [27]. The scattering and absorption cross sections of a spherical nanocluster in vacuum are given as the following [28]

$$C_{abs} = \frac{2\pi}{\lambda} Im\left[4\pi R^3 \frac{\varepsilon-1}{\varepsilon+2}\right] (2\text{-}1)$$

$$C_{sca} = \frac{1}{6\pi}\left(\frac{2\pi}{\lambda}\right)^4 \left|4\pi R^3 \frac{\varepsilon-1}{\varepsilon+2}\right| (2\text{-}2)$$

14

where, λ is the wavelength of the incident light, R is the nanocluster's radius and ε is the permittivity of the metal [29]. Equations (2-1) and (2-2) indicate that as the size of the nanocluster decrease the scattering of the incident light decrease and the absorption of the light increase up to maximum at a specific frequency termed as resonance frequency (ω) where $\varepsilon \simeq -2$. Moreover, for a spherical nanocluster in vacuum the scattering efficiency is given by

$$Q_{sca} = \frac{C_{sca}}{C_{sca} + C_{abs}} \ (2\text{-}3)$$

As a result of the excitations of surface plasmons at that frequency, the light interact with the nanocluster cross-sectional area because the polarizability $(4\pi R^3 \frac{\varepsilon - 1}{\varepsilon + 2})$ of the nanocluster becomes very high in this frequency range [30]. Extinction is dominated by absorption in metal nanoclusters due to the tendency of these nanoclusters to absorb more as their size get smaller than the wavelength of light and scatter more as their size get lager. For Ag nanoclusters with size less than 10nm the dominant process is the absorption which will increase the hole – electron pair photogeneration [31]. In addition, SPB of Ag nanoclusters is strong and a broad band was observed in absorption spectrum in the UV-visible spectrum [27]. Thus, silver nanoclusters can improve the light absorption in the visible range. Incident light that is in the region of the resonance frequency of the silver nanoclusters is strongly scattered or absorbed, depending on several parameters such as the diameter of the nanocluster, nanocluster shape and environmental forms [25, 32]. Therefore, a thin layer of silver nanoclusters on top of a thin-film solar cell

can improve its light absorption by reducing the reflection at the top surface of a solar cell from the entire light absorbing spectra [22, 30].

2.3 Studies on the fabrication of silicon and silver nanoclusters

Currently, semiconducting nanoclusters have great potential for the next generation of photovoltaic applications due to their low cost and easy fabrication, which make them suitable for large-scale manufacturing [33]. Many different approaches have been proposed in exploring the nano-scale level of silicon and its application in the field of photovoltaic solar cells by investigating their size distributions and their size dependent properties [34 - 36]. By controlling the size of Si nanoclusters, researchers can alter their surface properties to suit their needs and to enhance the solar cell efficiency. Thus, many efforts have been directed to the fabrication of Si and Ag nanoclusters.

Spencer et al. [37] synthesized silicon nanoclusters at atmospheric pressure by ion-beam sputtering followed by short-period annealing of silicon-on-insulator substrates to temperatures ranging between 600 and 900 °C in argon. Additionally, two different thin film layers were deposited: thin 6 nm layer samples were annealed for 30 s, and thick 15 nm layer samples were annealed for 60 s. Through imaging both sets of samples by an atomic force microscopy (AFM),, nanoclusters were observed to form at all the anneal temperatures. It was found that the average nanocluster size increased with increasing both anneal temperature and duration.

Silicon nanoclusters were produced by CO_2-laser-induced decomposition of silane in a flow reactor and early extraction of the reaction products into high vacuum by Huisken et al. [38]. Time of flight (TOF) mass spectrometer, SEM, AFM, Raman and photoluminescence (PL) spectroscopy have been used to characterize the nanoclusters in the gas phase or deposited as isolated nanoclusters and thin films on various substrates.

Si nanoclusters were also deposited using multi-hollow plasma chemical vapor deposition (CVD) was reported by Shinya el al. [39]. The produced films have a wide optical band gap of 1.75 eV and a large absorption coefficient. Their results indicated that nano-crystalline Si films are promising materials for solar cells.

The research group of Munir Nayfeh at University of Illinois [18] deposited Si nanoclusters in the range of 1 – 3 nm directly onto polycrystalline Si solar cell by dispensing particles from a volatile solution over the cell. Consequently, the solar cells light absorption has been enhanced by 60 % in the ultraviolet range, heat generation has been reduced and the time life of the solar cell has been extended. When the silicon nanocluster size was increased to 2.85 nm, the light absorption of the solar cell was improved by 10% in the visible light spectrum. The enhancement is due to the direct band edge absorption of Si nanoclusters. Nayfeh and co-authors [18], dispersed silicon nanoclusters of desired sizes dissolved in alcohol onto the of the solar cell surface and then, after

the evaporation of alcohol, a thin film of nanoclusters was spotted on top of the solar cell surface.

Silver nanoclusters production by irradiating Ag target with a 532-nm laser beam in pure water has been reported by Pyatenko et al. [40]. They were able to synthesize very small spherical nanoclusters with a mean size of 2 – 5 nm by working with high laser power, small spot sizes and controlled ablation time. The influence of those factors were studied, also the possible mechanisms of nanocluster formation are discussed.

Silver nanoclusters were synthesized by means of inert gas condensation and co-condensation techniques by Baker et al. [41]. Evaporation of a metal into an inert atmosphere with the subsequent cooling for the nucleation and growth of the nanoclusters is the basis of those techniques. Additionally, the antibacterial efficiency of the nanoclusters was investigated by introducing the nanoclusters into a media containing Escherichia coli.

Pillai, et al [30] have investigated the suitability of localized surface plasmons on Ag nanoclusters generated by thermal evaporation of Ag followed by annealing for the sake of enhancing the absorbance of thin-film and wafer-based solar cells. They found that the surface plasmons could increase the spectral response of solar cells over almost of the entire solar spectrum. It was observed that at wavelengths close to the band gap of Si, a significant enhancement of the absorption occurs. Also, it was reported a 7-fold enhancement for wafer-based cells at λ = 1200 nm up to 16-fold enhancement at λ = 1050 nm for 1.25 µm thin silicon on insulator (SOI) cells. In addition, 33% increase of the total current of the

18

device when averaged over the AM1.5 global radiation for Ag nanocluster layer of thickness about 12 nm and 16% increase for clusters sizes of 16 nm Ag thickness were observed. They also reported a close to 12-fold enhancement in the electroluminescence from ultrathin SOI light-emitting diodes and investigated the effect of varying the Ag nanocluster size on that enhancement. It was found that smaller metal nanoclusters provide maximum overall enhancement in the visible as well as the near-infrared for solar cell applications.

Ag nanoclusters with 5 nm diameter have been used to increase photocurrent response in tandem organic solar cells [42]. Ag nanoclusters were deposited at a rate of 0.5 Å/s to a thickness of 1 nm and the absorption spectra were measured on quartz substrates using a UV visible spectrometer. The enhancement of an incident optical field reaches into an organic dielectric for distances of up to 10 nm from the Ag nanocluster layer. Rand et al. [42] investigate the role that nanocluster spacing, shape, and an embedding dielectric medium with a complex dielectric constant play in determining plasmon enhancement. A dramatic increase in the efficiency of tandem organic solar cells due to the 1 nm Ag nanocluster layer was reported.

Beck et al. [22], deposited Ag films with a thickness of 14 nm by thermal evaporation at a background pressure of less than 3 Torr and annealed at 260 °C for 30 minutes on different substrates. Upon heating the thin Ag films break up under surface tension to form isolated nanoclusters; the size, density and shape were found to be dependent on

the substrate due to the variation in surface conditions between sample types. They have demonstrated an effective method of enhancing light trapping in solar cells with thin absorber layers by tuning localized surface plasmons in arrays of Ag nanoclusters. By redshifting the surface plasmon resonances by up to 200 nm through the modification of the local dielectric environment of the nanoclusters, an increase in the optical absorption in an underlying Si wafer 5-fold at λ =1100 nm and enhancement in the external quantum efficiency of thin Si solar cells by a factor of 2.3 at this wavelength were observed. Ultimately, they designed Ag nanoclusters to target specific wavelength regions where light trapping is need.

In addition, Sirbu and his group [43] deposited Ag nanoclusters electrochemically on the surface of the GaP substrate. Formation of Ag nanoclusters with mean size of 30 - 40 nm was controlled by 2 minutes electrochemical deposition followed by thermal processing at 400 °C for 1 hour. Additionally, they have studied the Ag nanoclusters' surface plasmon resonance. It was observed that the plasmon resonance frequency of metallic nanoclusters is highly sensitive to the refractive index of the medium they are incorporated into. Moreover, it was shown that porous templates provide wide possibilities for the control of surface plasmon resonance frequency of metallic nanoclusters, since the effective refractive index of the template can be varied from the value of the bulk material refractive index to values around one or even lower than one by changing the porosity and morphology.

Moreover, Srivastava et al. [44] have developed a relatively simple and fast process for nano-texturing of p-Si surface using Ag-catalyzed wet

20

chemical etching in aqueous HF and hydrogen peroxide ($H_2 O_2$) solution at room temperature to minimize the reflection losses of the solar cell. Reflectivity less than 4% can be reported in the usable spectral range for silicon solar cells. Larger than 20% improvement in the short circuit current density and 1.25% efficiency has been achieved in the nano-textured-silicon solar cells compared to the planar cell due to the increased in the surface to volume ratio of the nano-textured surface compared to the planar cell.

2.4 Inert gas condensation technique

As explained in the previous section, there are different techniques for the synthesis of Si and Ag nanoclusters. Nanocluster synthesis by physical vapor deposition (PVD) is one of these techniques and was first introduced by Granqvist and Burman [45]. PVD processes used to describe any of a diversity of techniques to deposit thin solid films of by the condensation of a vaporized atoms or clusters of the solid material onto various surfaces and substrates. PVD comprises a wide range of vapor phase methods such as thermal evaporation, electron beam (e-beam) and sputtering. However, thermal evaporation has a known limitation to be used for metals and intermetallic compounds. This limitation was overcome later by Hahn and Averback [46] by substituting the thermal evaporation source with a sputtering source, thus enabling the synthesis of nanoclusters. However, the size of these nanoclusters depended on the

pressure of inert gas in the operating chamber such that a small change in the pressure would change the nanocluster size.

The nanoclusters presented in this work were fabricated using magnetron sputtering process combined with inert gas condensation. The sputtering process was first report by in 1852 Grove [47] and since then it has been used in different fields. Atomic vapor produced by magnetron sputtering results from the ejection of the metal atoms from the target surface due to momentum transfer associated with surface bombardment by energetic ions. A strong negative field is applied to the target to attract positive ions. The sputtered atoms flow across the vacuum chamber to where they deposited [48]. The advantages of this technique are: 1) thickness uniformity over large area, 2) good control of film thickness, 3) cleaning of the target surface prior the deposition process, and 4) deposited material maintains the stoichiometry of target composition.

Inert gas condensation (IGC) is a process in which atomic vapor condenses inside a chamber (source chamber) using an inert gas such as helium or argon at low partial pressure (in the current study we used argon). Upon contact, the inert gas condenses atomic vapor, carries the condensed particles outside the source chamber due to the pressure difference, deposits them on a substrate, and produces uniformly deposited nanoclusters. The vapor of the metal atoms loses its kinetic energy due to interatomic collision with inert gas atoms and condenses to form nanoclusters. Inert gas condensation can be used to synthesis nanoclusters of almost any material that can be sputtered by a magnetron

22

gun or vaporized by thermal evaporation. Figure 7 shows a schematic illustration of nucleation and growth of nanoclusters by inert gas condensation technique.
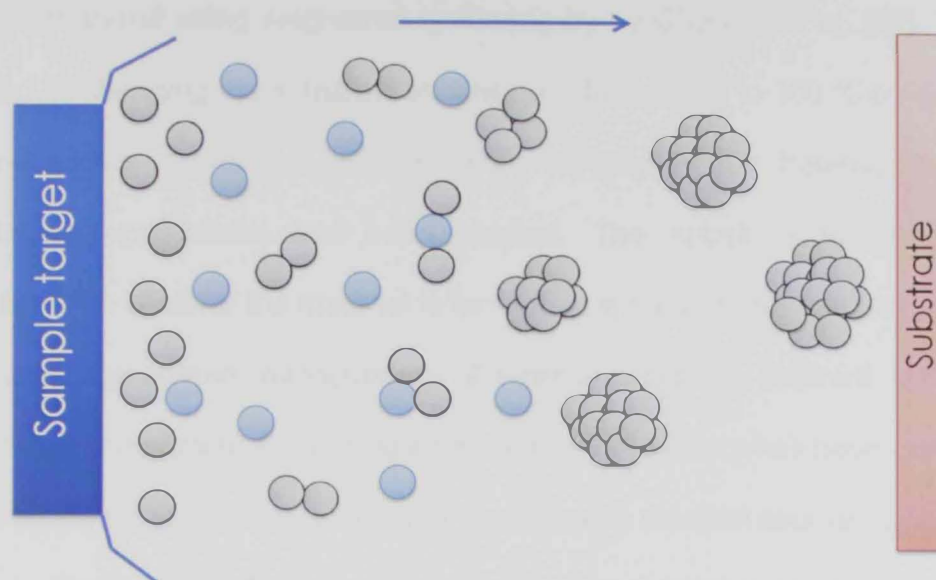
Fig. 7. A schematic illustration of inert gas condensation, with the sputtered atoms (gray color) colliding with inert gas atoms (blue color) to form nanoclusters.

In addition, the mean size of nanoclusters inside the source chamber is determined by the choice of synthesis parameters such as the flow rate of argon inert gas (f_{Ar}), the length in which the nanoclusters aggregate (L) and sputtering discharge power (P) [49].

2.5 Studies on nanoclusters synthesized using IGC technique

Among the different techniques for nanocluster production, inert gas condensation is a favorable technique due to the high level of control on the size and properties of nanoclusters, and the wide range of materials that can produced using this technique. Efforts have been made to

23

optimize the process conditions to produce nanoclusters with specific properties for various applications.

Nanoclusters of silver with size range of 3 nm up to 60 nm were prepared using magnetron sputtering by by Chandra et al. [50]. The effect of changing the substrate temperature from 70 °C to 300 °C on silver nanoclusters produced by magnetron sputtering for heterogeneous catalysis applications has been studied. The substrate temperature determines whether the material is formed as a nanocluster thin film or as loosely aggregated nanoclusters. Characterization of different growth patterns and particle morphologies of silver nanoclusters has been carried out by atomic force microscopy and transmission electron microscopy.

Raffia et al. [51] have synthesized Ag nanoclusters by an IGC method using helium inert gas in the source chamber. Nucleation, growth mechanism and the kinetics of nanocluster synthesis in vapor phase were studied. They found that the evaporation temperature and inert gas pressure have a great influence on nanocluster crystallinity, morphology, and size distribution. Nanoclusters were synthesized using evaporation temperatures of 1123, 1273, and 1423 K; and at helium pressures of 0.5, 1, 5, 50, and 100 Torr. X-ray diffraction (XRD) and TEM were used to characterize the synthesized Ag nanoclusters. The nanocluster size ranged from 9 to 32 nm, depending on the growth conditions.

In addition, Pérez et al. [52] have fabricated gold/palladium nanoclusters by IGC using a sputtering source with nozzles of sizes 1, 3, and 5 nm on size, depending on the choice of the synthesis conditions. The structure and size of the Au/Pd nanoclusters were determined by

24

mass spectroscopy, and confirmed by AFM and TEM measurements. In addition, the chemical composition was analyzed by X-ray microanalysis.

Banerjee, Krishna and Das [35] at Nevada Nanotechnology Center synthesized copper (Cu) and silicon nanoclusters by a sputtering and inert gas condensation type growth technique. They found that the size distributions of the nanoclusters follow a normal distribution. And the variation of nanocluster size is dependent on several parameters, such as the length in which the nanoclusters aggregate, the flow rate of the aggregation gas and the pressure of the aggregation region. They have observed a variation in the average nanocluster size with the variation of the inert gas (argon) flow rates. They concluded that proper adjustment of operation conditions could lead to desired nanocluster size distributions.

Miguel et. al. [53] silver nanoclusters were synthesized using the inert gas aggregation technique with different average sizes: 1.3 ± 0.2, 1.7 ± 0.3, 2.5 ± 0.4, 3.7 ± 0.4, 4.5 ± 0.9, and 5.5 ± 0.3 nm. Also, they concluded that it is possible to produce silver nanoclusters with icosahedral shape, hence, controlling not only the size but also the shape. Consequence, they suggested the possibility of changing the properties for the icosahedral shape as a function of size.

Ayesh et al. [34] have synthesized palladium (Pd) nanoclusters using a dc magnetron sputtering source of mean size between 2 to 10 nm. Ayesh's main objective was to investigate the variation in Pd nanoclusters' properties as their sizes increase in order to understand the evolution of the physical and chemical properties with the growth from atoms to bulk. They investigated the dependence of Pd nanoclusters' size distribution on

different source factors, such as the sputtering discharge power, inert gas flow rate (f_{Ar}), and aggregation region length (L). It was found that the inert gas flow rate and aggregation length have the major effect on determining the nanocluster size. In addition, it was observed that increasing L leads to a formation of large nanoclusters due to the increase in the nucleation time (time nanocluster needed to grow).On the other hand, the nanocluster peak diameter variation with f_{Ar} reveals two nucleation mechanisms: nucleation of new small nanoclusters which leads to a decrease in the nanocluster size with f_{Ar}; and nucleation of large nanoclusters where the nanocluster size increases as f_{Ar} increases.

The mechanism of nanoclusters formation has been analyzed by Knauer, Hihara, Ayesh, and Banerjee [18, 34, 35, 54, 55] groups research on experimental results and theoretical principles of two-body and three-body collisions. A theoretical model for the formation of metal and semiconductor nanoclusters by homogeneous nucleation and collision growth in the vapor phase was introduced by Knauer [54]. Knauer's model describes nanocluster nucleation and growth by growing embryos initiated via three-body collision in the growth region into large nanoclusters by a two-body collision. Therefore, when stable embryos are made by atomic collisions, they grow up to larger nanoclusters. Presence of nucleation centers such as argon atoms is a crucial factor to form nanoclusters by removing the excess kinetic energy between the sputtered atoms through three-body collision. The model was used to explain the growth of nickel, copper, silicon, and palladium nanoclusters produced using magnetron

sputtering sources [18, 34, 35, 54, 55]. Using the conservation of momentum principle, the nanocluster growth rate can be expressed as:

$$\frac{di}{dt} = \upsilon_z \frac{di}{dz} = \pi (r_c + r_a)^2 n \upsilon_{th} \beta \quad (2\text{-}4)$$

Where i is the number of atoms per nanocluster, z is the nanocluster traveling length, υ_z is the vapor velocity, r_c and r_a are the radii of nanocluster and atom respectively, n is the vapor density $\left(n = \dfrac{p}{k_B T} \right)$, υ_{th} is the mean velocity with the reduced mass of the i-sized nanocluster, and due to the high latent heat of condensation of metals many atoms must be condensed and evaporated again before a new atom can be retained by cluster then, β is introduced as the growth-retarding effect [54]. Equation (2-4) can be expressed in term of Mach number (M)

$$M = \upsilon_z \left(\frac{\gamma k_B T}{m_a} \right)^{1/2} \quad (2\text{-}5)$$

Where T is the temperature in Kelvin, k_B is Boltzmann constant, m_a is the mass of the vaporized atom, and γ is the ratio of specific heat of a gas at a constant pressure to heat at a constant volume.

and the following approximations are also made,

$$\frac{1}{m_*} = \frac{1}{m_c} + \frac{1}{m_a} \cong \frac{1}{m_a} \quad (2\text{-}6)$$

$$r_a + r_c \cong r_c = \left(\frac{3}{4\pi} \right)^{1/3} i^{1/3} a_\upsilon \quad (2\text{-}7)$$

Where a_υ is the interatomic distance $(a_\upsilon = 2r_a)$. Hence, integrating Eq. (2-4) gives

$$i^{1/3} = i_o^{1/3} + \left(\frac{4\pi}{3}\right)^{1/3}\left(\frac{1}{2\pi\gamma}\right)^{1/2} a_\upsilon^2 \int\limits_{z=0}^{\infty} \frac{\beta n}{M} dz \quad (2\text{-}8)$$

Where i_o is the size of a critical embryo and along the free jet n and M

vary according to the following approximations

$$n \cong \frac{1}{4} n_o \left(\frac{L}{d}\right)^{-2} \quad (2\text{-}9)$$

and

$$M \cong 3 \left(\frac{L}{d}\right)^{2/3} \quad (2\text{-}10)$$

Where d is the nozzle diameter, L corresponds to z in Eq. (2-8) and

$n_o = \frac{p}{k_B T}$ where p is the source pressure.

Evaluating of Eq. (2-8) gives

$$i = \left[i_o^{1/3} + \left(\frac{4\pi}{3}\right)^{1/3}\left(\frac{1}{2\pi\gamma}\right)^{1/2} a_\upsilon^2 n_o \beta_o \left(\frac{1}{M_o} + 0.1d\right)\right]^3 \quad (2\text{-}11)$$

In summary, different approaches have been proposed in exploring the nanoscale level of silver and silicon materials and their applications in the field of photovoltaic solar cells by investigating their size dependent properties. By controlling the size of Ag and Si nanoclusters, researchers could alter their properties to suit their needs and to enhance the solar cell efficiency.

CHAPTER THREE: EXPERIMENTAL PROCEDURE

3.1 Materials

Silicon targets with 99.999% purity in addition to silver targets with 99.99% purity were used as the sources of Si and Ag nanoclusters. Argon gas with 99.999% purity at different flow rates (f_{Ar}) was used to generate the plasma and to aggregate Si and Ag nanoclusters from their targets.

3.2 Apparatus

A nanocluster source (NanoGen50) from Mantis Deposition Ltd. (Oxfordshire, UK) was used to generate Si and Ag nanoclusters inside an ultrahigh vacuum (UHV) compatible system. The UHV system including the NanoGen50 source are shown in Fig. 8. Two turbo pumps with a backing pump were used to evacuate the main and source chambers to a base pressure of 10^{-8} mbar, as shown in Fig. 9. Argon inert gas at a different flow rates in the range of 10 - 90 SCCM was introduced inside the NanoGen50 using a mass flow controller (MFC) from MKS Instruments to generate the plasma and to aggregate Si and Ag nanoclusters from their targets which were fixed on a magnetron sputter head individually. Note that SCCM denotes to standard cubic centimeter per minute. The dc magnetron type discharge was used to generate Si and Ag nanoclusters with a discharge power up to 65 W. The magnetron gun and walls of source chamber were water-cooled. MesoQ quadrupole mass filter (QMF) was used in line with the NanoGen50 to analyze the nanocluster size and filter them.
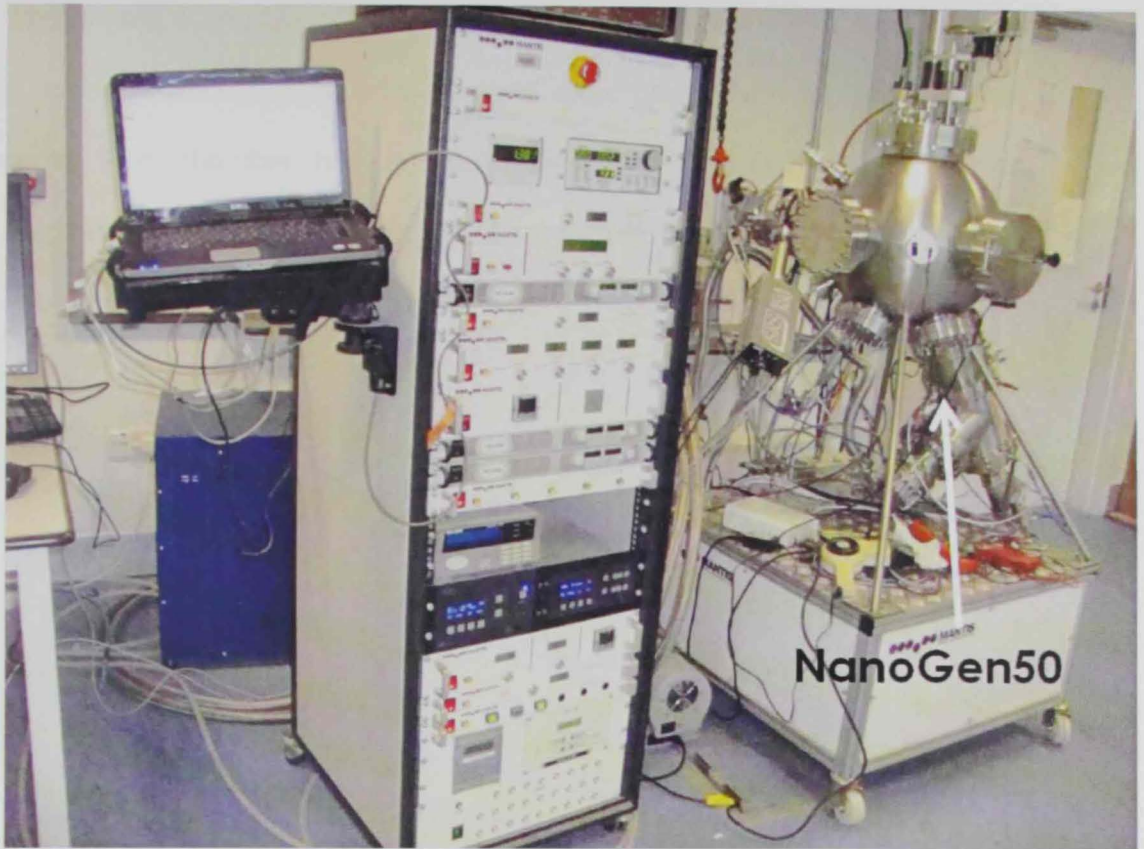
Fig. 8. UHV system for nanocluster production.

The major part in the UHV deposition system is the nanocluster source where the target is fixed on a magnetron sputter head, then nanoclusters are generated inside the source chamber and drifted to the main deposition chamber to be deposit onto a suitable substrate. The nanocluster source consists of: 1) a dc magnetron sputtering head combined with a linear motion drive as the one shown in Fig. 10, enabling the aggregation length L (L is the distance from the sputtering target surface to the source exit nozzle) to be adjusted up to 100 mrn inside the aggregation region; 2) two nozzles with diameters of 5 and 6 mm in order at the exit of the source chamber (inset of Fig. 9); 3) a water cooling systems for the sputter head and source jacket and 4) a turbo pump with

dry backing pump [34 - 35], see Fig. 9. The main deposition chamber has a spherical construction with all ports axes passing through the centre-point. The chamber has internal welds and is polished to minimize outgassing. A schematic diagram of the system is shown in Fig. 9.
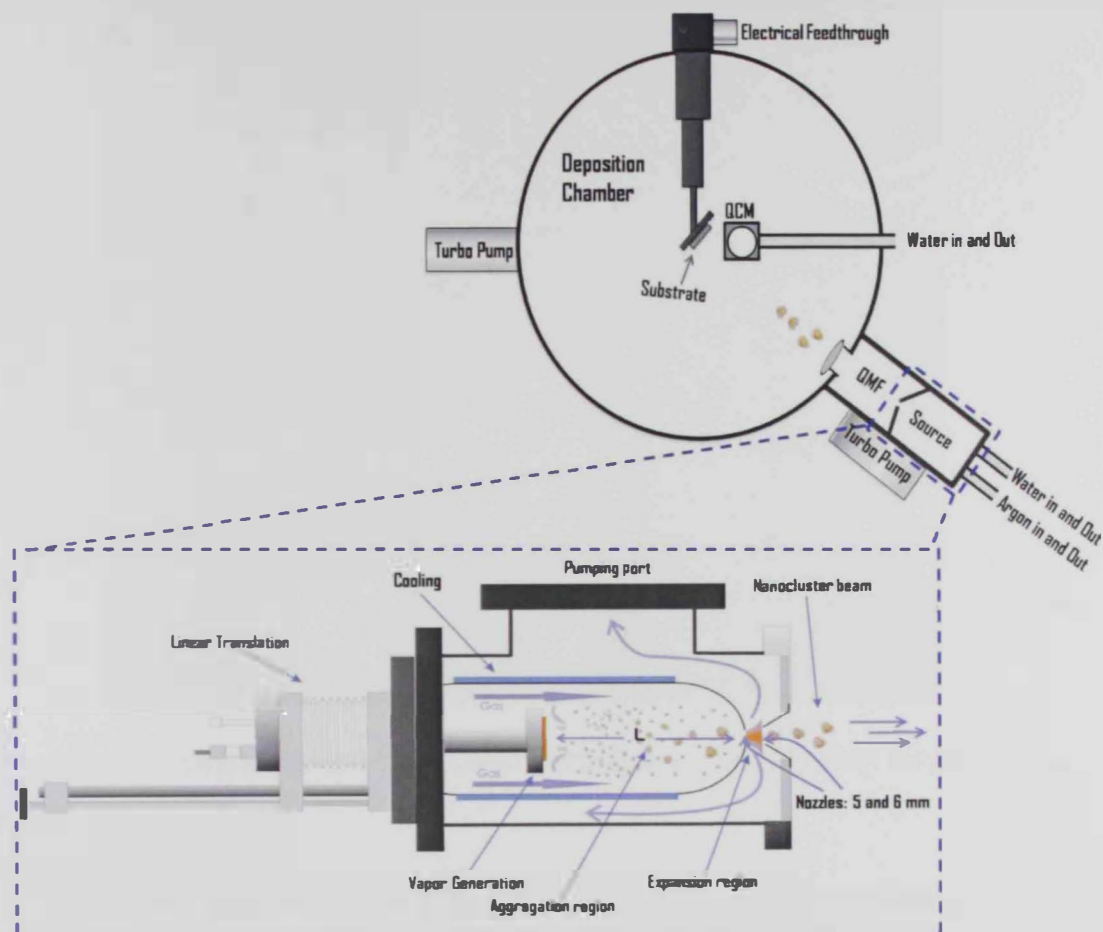
Fig. 9. Schematic illustration of the UHV system and NanoGen50 nanocluster source [34, 56].
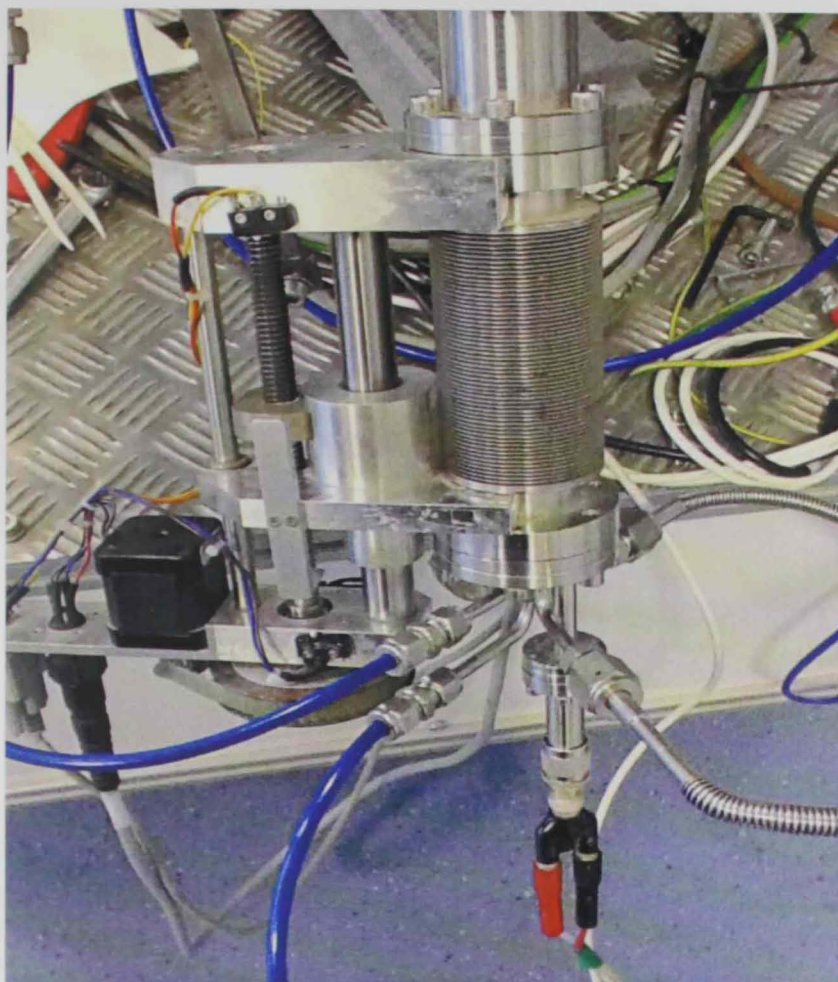
Fig. 10. Linear motion drive used to control the aggregation length.

Atoms sputtered from a target at room temperature by bombarding its surface with energetic ions. The magnetron gun used in the source provides wide range of nanocluster size range, which varies from fraction of a nanometer to few tens of nanometers [35]. Figure 11 shows the magnetron sputter gun with Ag target. The sputtered atoms or clusters travel through the source chamber in a reduced ambient pressure and get cooled down by argon gas, where these atoms/clusters nucleate to form a distribution of nanoclusters of various sizes depending on the residence

time within the aggregation region which can be varied by changing the aggregation length using the linear motion drive [30, 43].

Fig. 11. The magnetron sputter gun with Ag target.

A directed nanocluster beam is formed once the nanoclusters leave the 6 mm nozzle. The generated nanoclusters can be deposited on a substrate fixed on a sample holder that is mounted on a vertical linear motion drive. A quartz crystal monitor (QCM) and a controller module SQM 160 from INFICON, shown in Fig. 12 (a) and (b), were used to measure the nanoclusters deposition rate. To check the deposition rate, the sputtering crystal sensor is fixed on a linear motion drive to enable its transportation in front of the exit nozzle, and then pull it back away from the beam path as shown in Fig. 9. Without venting the system, the position of the linear motion drive holding the magnetron gun, sample holder and QCM can be controlled.

(a)

(b)
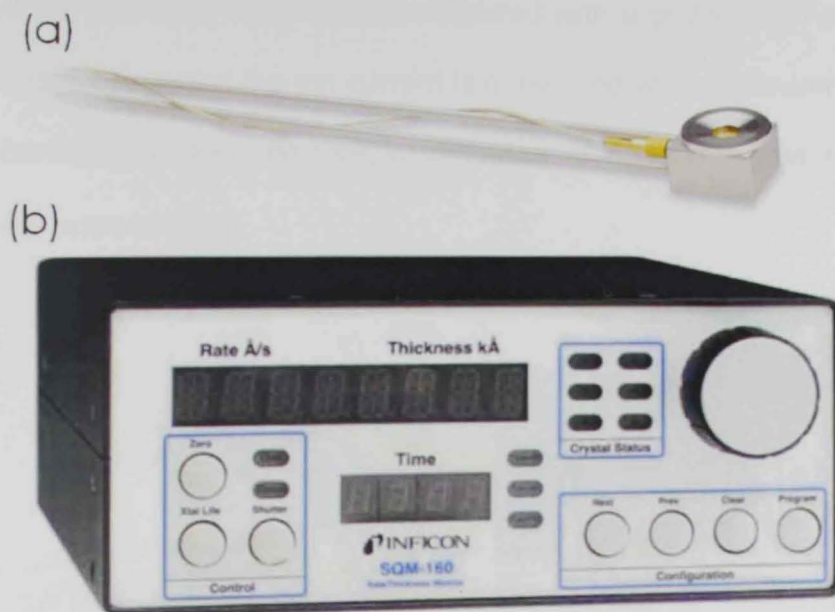
Fig. 12. High accuracy Quartz crystal (a) sensor and (b) monitor records
10 readings per second [57].

A quadrupole mass filter comprising of four identical cylindrical
metal rods set parallel to each other, schematically illustrated in Fig. 13
(a), was used to measure the nanocluster size distribution after they are
generated inside the source chamber. Each opposing rod pair is
connected together electrically to potentials equal in magnitude but
opposite in sign of $[U+V \cos(\omega t)]$ and $-[U+V \cos(\omega t)]$, where U is a direct
current (dc) voltage and Vcost is a radio frequency (RF) voltage. The ratio
U/V indicates the resolution of the quadrupole mass filter and was fixed in
each size distribution scan, and the mass distribution was scanned by
continuously varying the applied frequency, ω. The resolution of the
quadrupole mass filter is adjusted for a mass scan by setting the U/V ratio
up to 0.168 allowing precise particle size to be achieved. An experimental
configuration of a quadrupole mass filter is shown in Fig. 13(b). The ion

34

flux of the particular mass/size is measured with a grid located at the exit of the mass filter and the ion current is measured with a picoammeter. By maintaining U/V ratio constant, a spectrum of constant mass resolution M/ΔM is achieved [58].

(a)
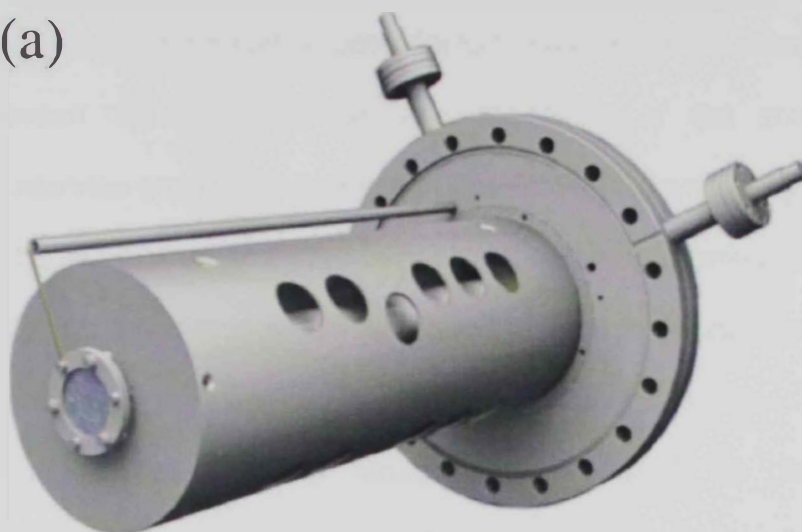
(b)

Fig. 13. (a) Schematic illustration [56] and (b) experimental configuration of a quadrupole mass filter.

3.3 Nanoclusters fabrication

Fabrication of silicon and silver nanoclusters using the dc plasma magnetron sputtering consists of the following steps: 1) evacuating the main and source cha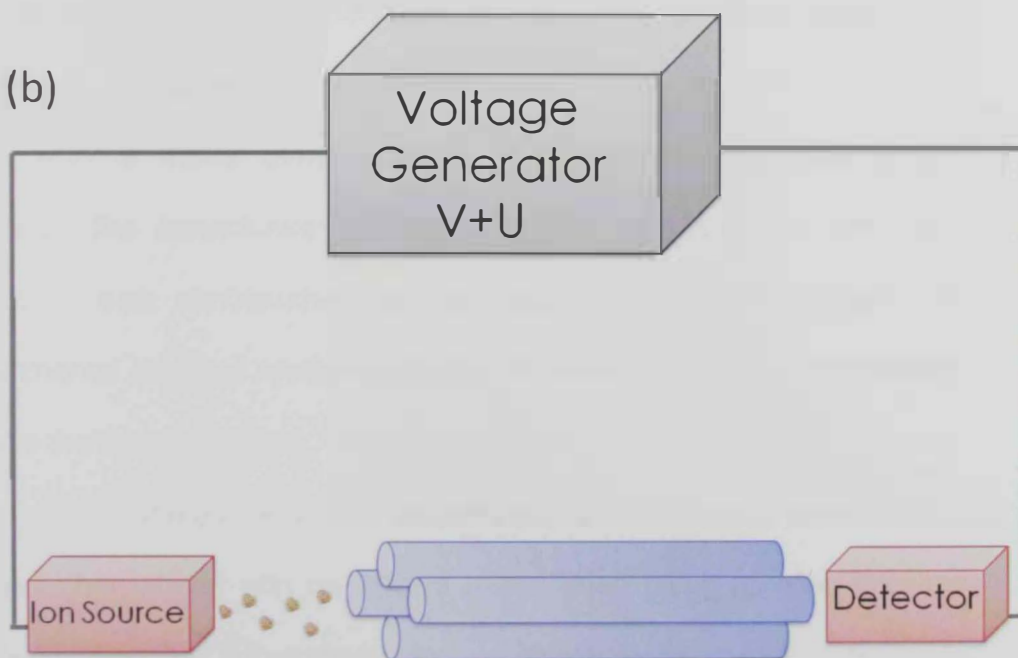mbers, 2) introducing argon inert gas inside the source chamber as the medium in which plasma is initiated and sustained when applying a negative potential to the target, 3) the potential difference between the biased target and the body of the source chamber accelerates argon ions to bombard the target and physically sputter atoms and small clusters from the target by transferring momentum to them and 4) the sputtered atoms and clusters pass through the discharge region and aggregate there where they lose their kinetic energy. The pressure difference between the source chamber and the main chamber accelerates the generated nanoclusters to the quadrupole mass filter to be mass scanned and then penetrate to the main chamber where they eventually get deposited on a substrate.

After a visible glow discharge is maintained inside the source chamber, the nanocluster deposition rate is monitored on the QCM controller, thus nanoclusters can be deposited on the substrate. The experimental steps of synthesis of films of silicon and silver nanoclusters involve the following steps:

1) Glass substrates were first sequentially cleaned using acetone and ethanol, then rinsed with de-ionized water, dried using nitrogen gas and finally fixed on the substrate holder, as shown in Fig. 14. The substrate holder was then fixed on the substrate table inside the main chamber.

36

2) The target was placed on the magnetron sputter head, and the source chamber and the system were sealed.

3) The two chambers were then evacuated to a pressure better than 1×10^{-6} mbar.

4) Argon inert gas valve was opened to the NanoGen50. (Efforts have been made to keep the system as clean as possible to avoid any contamination of the chamber and samples).

5) The QCM was moved to a position facing the source nozzle (to 20 mm) to be ready to measure the deposition rate.

6) Using control software of the UHV system (Virtual Rack), we set the discharge electrical current, adjust Ar flow rate and control the sputter head position to achieve desired deposition rate. Also the discharge voltage is monitored to calculate the sputtering discharge power.

7) Once a desirable deposition rate is achieved, the QCM was moved back away from the nanoclusters beam before starting nanocluster deposition.

8) The substrate shutter was opened to start deposition and count the deposition time. The shutter position is in front of the substrate allows pre-sputtering of the target to remove any oxides on the target surface prior to deposition. For fabrication of silicon nanoclusters, RF sputtering was used to remove the oxide from the silicon target surface for a 15 minute before applying the dc sputtering.

3.4 Characterization methods

The size distributions of silicon and silver nanoclusters were typically measured by analytical techniques such as quadrupole mass filter (QMF), transmission electron microscopy (TEM)

TEM studies were conducted using a Philips CM10 TEM microscope. In order to determine the size of individual Si and Ag nanoclusters, TEM images of Si and Ag nanoclusters directly deposited on carbon-coated copper TEM grid at ambient temperature were used and kept in the evacuated system up to the test day, as shown in Fig. 14.

Fig.14. Substrate holder that include TEM grids. The dimeter of the substrate holder is 5 cm.

The MesoQ quadrupole mass filter was used in line with the NanoGen50 source to filter and study the nanocluster size distribution.

First of all, one must select the target material. After that, adjust the resolution of the QMF by setting U/V ratio. Next a mass scan can be performed; then the data can be saved by setting and enabling scan log file.

3.5 Analysis methodology

3.5.1 Origin software

The format of the size distribution log files from MesoQ software's was changed to be used in origin software. Using origin software, both the average size of nanoclusters and area under the size distribution curves (the area under a size distribution curve her represents the number of nanoclusters) were measured by cutting the reference and setting start and end points for each size distribution. The average nanocluster size and standard deviation were measured for each size distribution to study the dependence of nanoclusters' average size on various source parameters, such as: sputtering discharge power, aggregation length, and inert gas flow rate. In addition, the number of nanoclusters was measured for size distributions produced using various source parameters (sputtering discharge power, aggregation length, and inert gas rate) by integrating the area under each size distribution curve.

3.5.2 TEM images

The confirmation of size distribution for silicon and silver nanoclusters measured by the quadrupole mass filter was performed by transmission electron microscope. A relative nanoclusters size was

measured using TEM images by measuring the diameter by a ruler and converting the result to its real size (the scale used here depends on the magnification of the TEM image).

CHAPTER FOUR: RESULTS AND DISCUSSION

4.1 Results

The U/V ratio effect on the size distribution of Ag nanoclusters synthesised using a discharge power of 21.3 W, f_{Ar} = 60 SCCM, and L = 70 mm is shown in Fig. 15. The figure illustrates that as the U/V ratio increases from 0.1 to 0.16 the nanocluster intensity signal decreases, and the size distribution shows various structures.
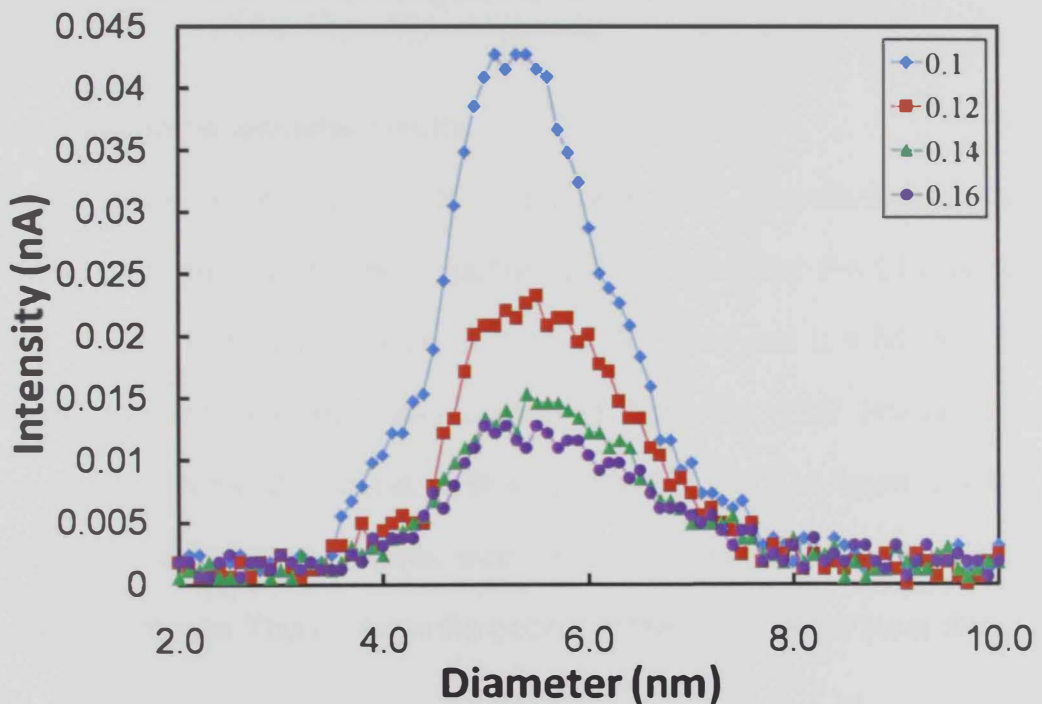

Fig. 15. U/V ratio effect on the nanocluster size distribution for Ag nanoclusters.

Nevertheless, the size distributions stays within the range of 3.3–8.1 nm as the U/V ratio changes. Also the average nanocluster size remain constant at 5.4 nm. This confirms that the performance of the current mass filter is decent.

The decrease of the intensity of the size distrbution by increasing the U/V ratio indicates the formation of narrow size range of nanoclusters. U/V ratio of 0.12 generates a reasonably strong signal while maintaining the distribution structures; hence it is used for the rest of this work.

Nanocluster size distribution varies with the variation of various parameters, such as the flow rate of inert gas, the length in which the nanoclusters aggregate, and sputtering discharge power. Therefore, it is the objective of this work to analyze and understand this variation.

4.1.1 Silicon nanocluster results

Figure 16 shows a TEM image with high magnification of Si nanoclusters generated using a sputtering discharge power P = 21.2 W, f_{Ar} = 90 SCCM, chamber pressure of 2.08 x 10^{-3} mbar and L = 80 mm. Si nanocluster average size was measured from the TEM image and compared with the QMF result as illustrated in Fig. 17 . The figure reveals reasonable agreement between size distributions measured using QMF and TEM images. This confirms the decent performance of the mass filter.
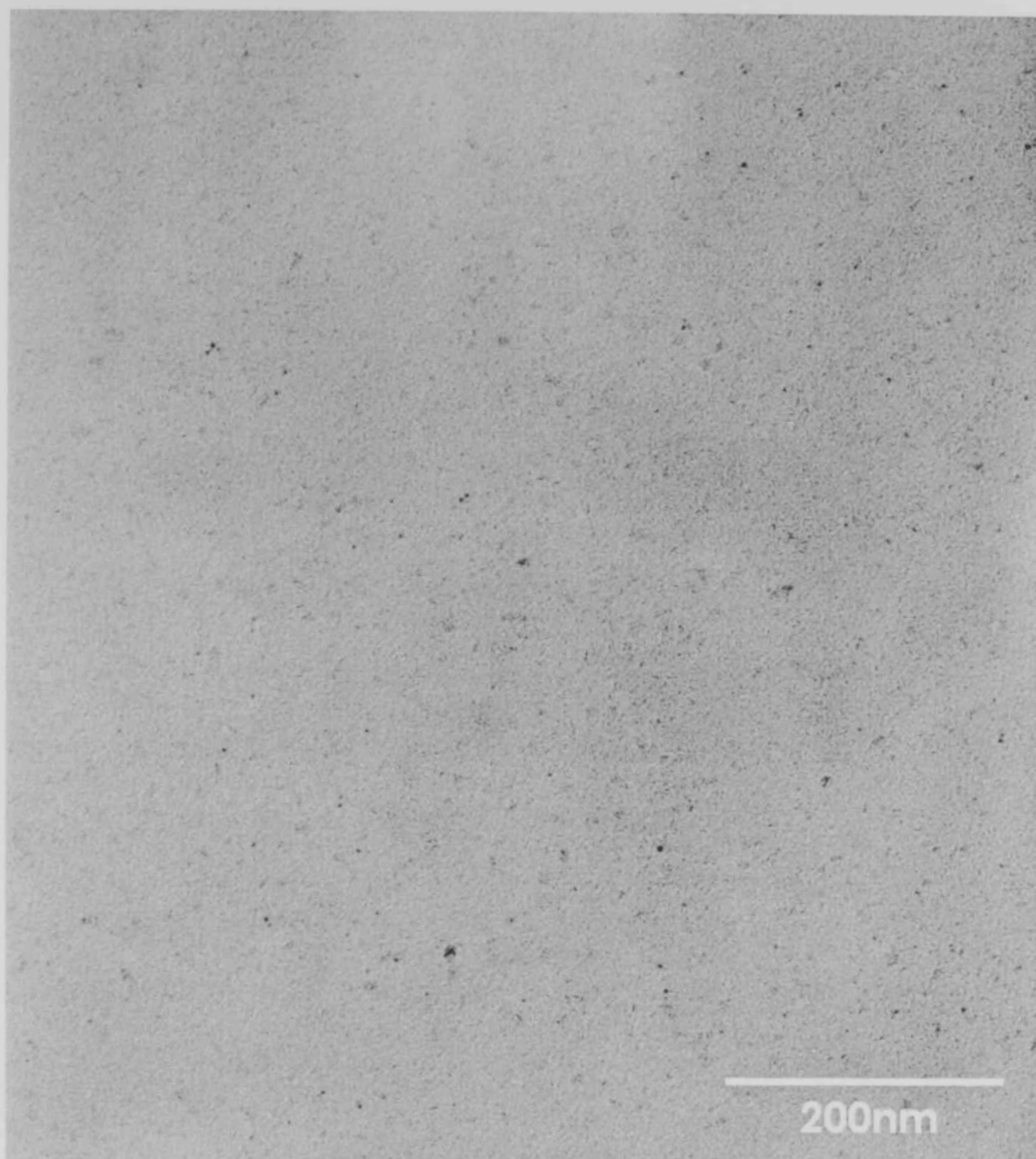
Fig. 16. TEM image of Si nanoclusters (P = 21.2 W, fAr = 90 SCCM and L = 80 mm).
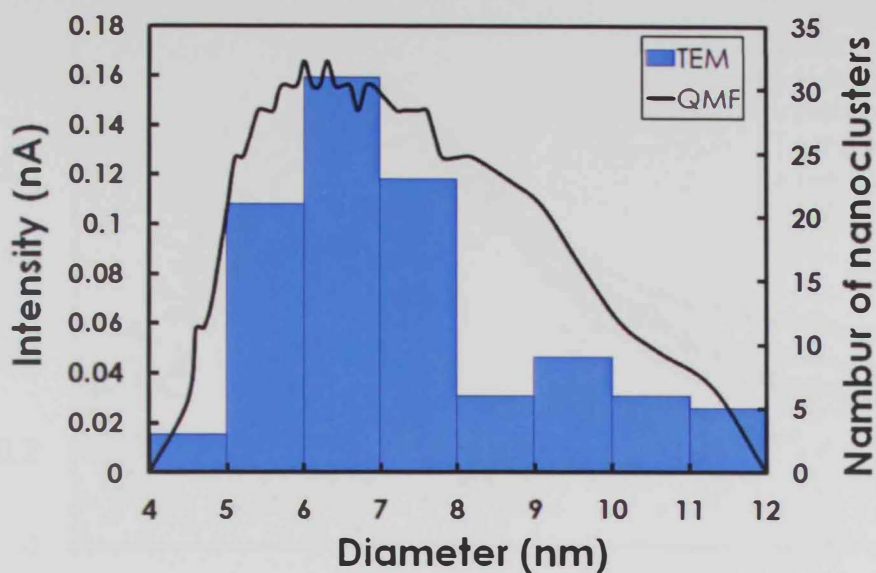
Fig. 17. Comparison of size distribution of Si nanoclusters
(P = 21.2 W, fAr = 90 SCCM and L = 80 mm) measured using the QMF
(solid line) with that measured using TEM (histogram) for nanoclusters
deposited under the same conditions.

Figure 18 shows size distribution curves of Si nanoclusters

generated using a 64.4 W sputtering discharge power, Ar flow rate of 30

SCCM and chamber pressure of 6.25×10^{-4} mbar for different aggregation
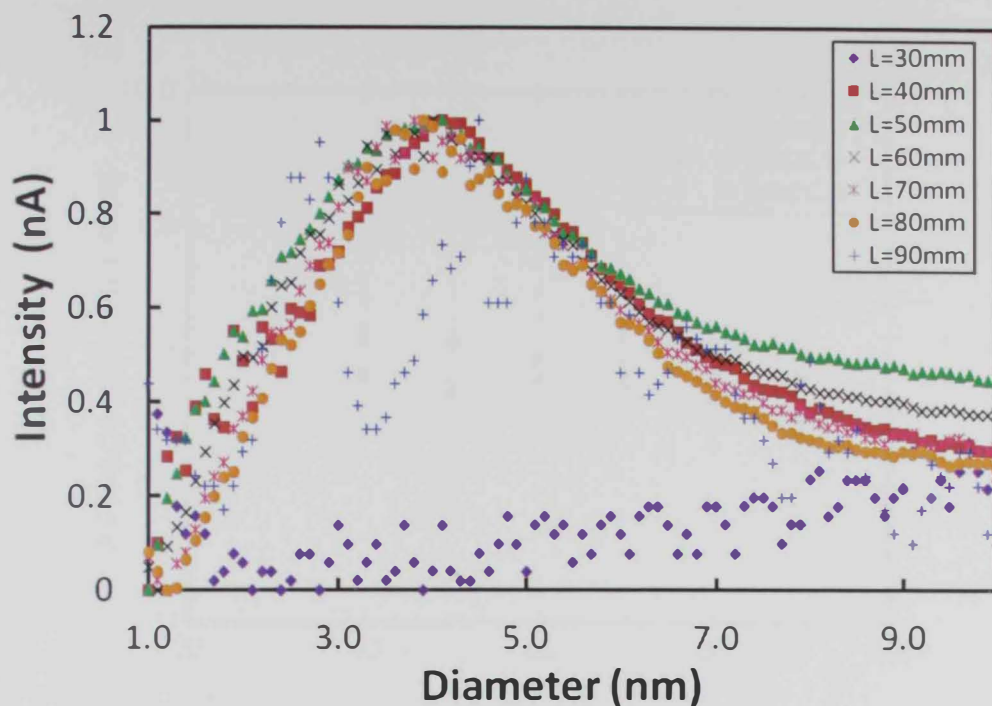
lengths.

Fig. 18. The dependence of the size distribution of Si nanoclusters on the aggregation length L in the range of 30 mm up to 90 mm.

The produced nanoclusters exhibit the same average nanocluster size of 4nm with increasing the aggregation and maintaining the same nanocluster yield. Figures 19 (a) and (b) show the dependence of Si nanoclusters' average size and yield on the aggregation length for different Ar flow rates. The results are generated using a 28.9 W discharge power and pressure in the range of $6.2 \times 10^{-4} - 1.12 \times 10^{-3}$ mbar. Each error bar in the figures is the standard deviation of the size distribution curve. The small standard deviation indicates that narrow size distributions of nanoclusters are formed. Figure 19 (a) shows that the nanocluster average diameter is approximately constant within the error bars in the range of 3.5nm to 5.3 nm. The weak dependence of the average size on L could be a result of inefficient cooling of the Ar inert gas.
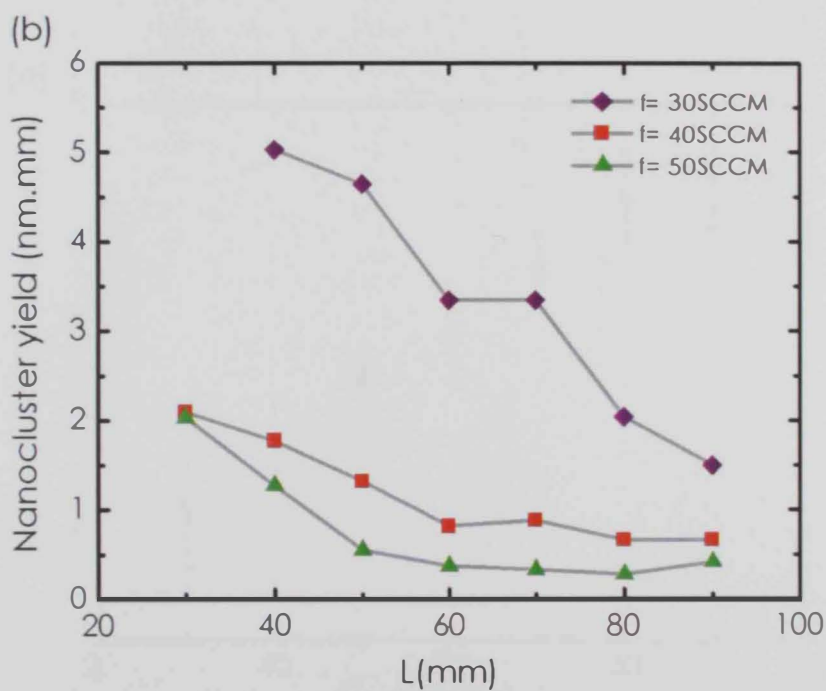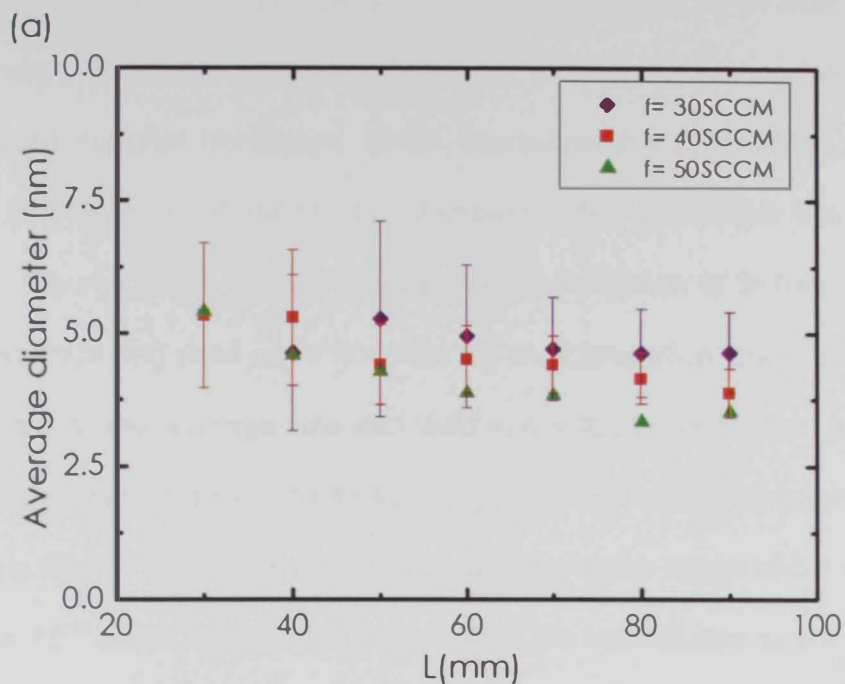
Fig. 19. The dependence of Si nanocluster (a) average size, and (b) area under the size distribution curves on the aggregation length for Ar flow rates between 30 and 50SCCM.

On the other hand, Fig. 19 (b) shows that increasing the

aggregation length decreases the area under each size distribution curve

which is indicating a decrease of the nanocluster yield for Ar flow rates in the range of 30 up to 50 SCCM. As L increases, the density of the sputtered material decreases which decreases the probability of three-body and two-body collisions, thus decreasing the nanocluster yield.

Figures 20 (a) and (b) illustrate the dependence of Si nanoclusters' average size and yield on Ar flow rate for an aggregation length of 90 mm. The nanocluster average size and yield in the figure were taken from size distribution curves similar to those in Fig. 18. The results were generated using a 28.9 W discharge power and pressure in the range of 6.2×10^{-4} – 2.05×10^{-3} mbar. Figure 20(a) shows that the nanocluster size increases with increasing f_{Ar}.

(a)

(b)
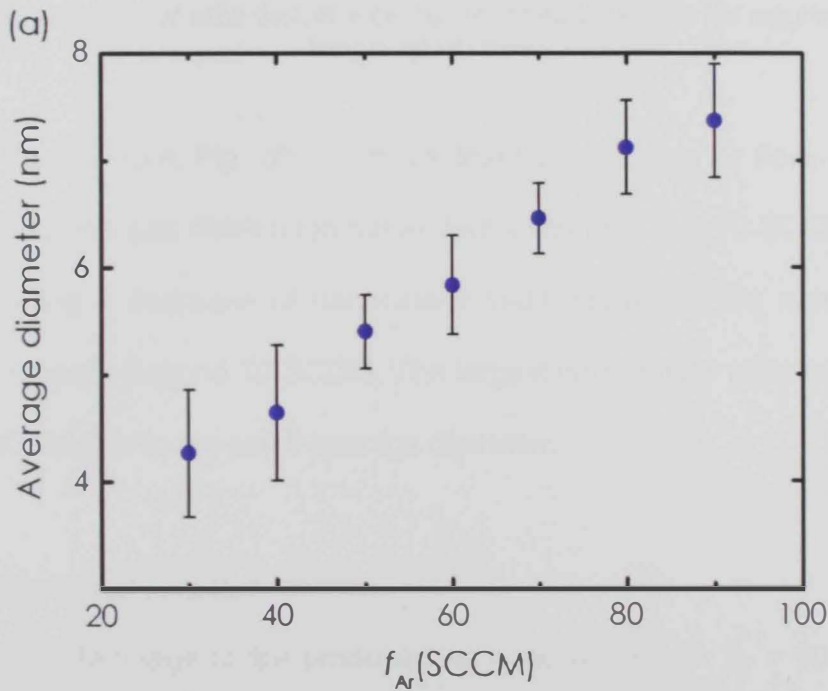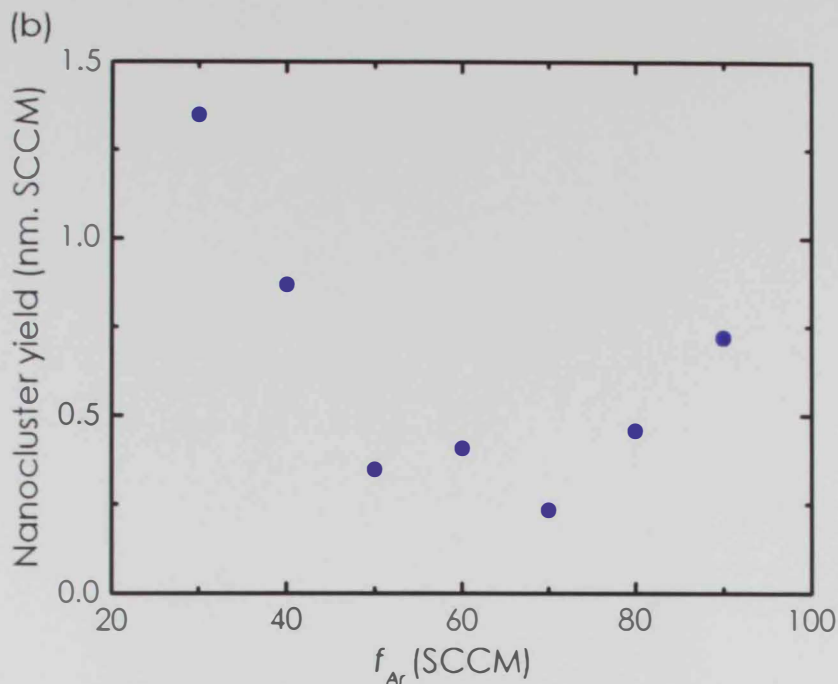
Fig. 20. The dependence of Si nanocluster's (a) average size and (b) area of the nanocluster size distribution curve on Ar flow rate for aggregation length of 90 mm.

Furthermore, Fig. 20 (b) shows that by increasing Ar flow rate, the area under the size distribution curve decreases until f_{Ar} = 70 SCCM which is indicating a decrease of nanocluster yield. However, the nanocluster yield increases beyond 70 SCCM. The largest nanocluster yield was for f_{Ar} = 30 SCCM due to the small average diameter.

4.1.2 Silver nanocluster results

A TEM image of the produced Ag nanoclusters for f_{Ar} = 60 SCCM, pressure of 1.37×10^{-3} mbar, P = 21.45 W and L = 70 mm is shown in Fig. 21. From the TEM image, the average size was measured and it is shown in Fig. 22 (the histogram).

48
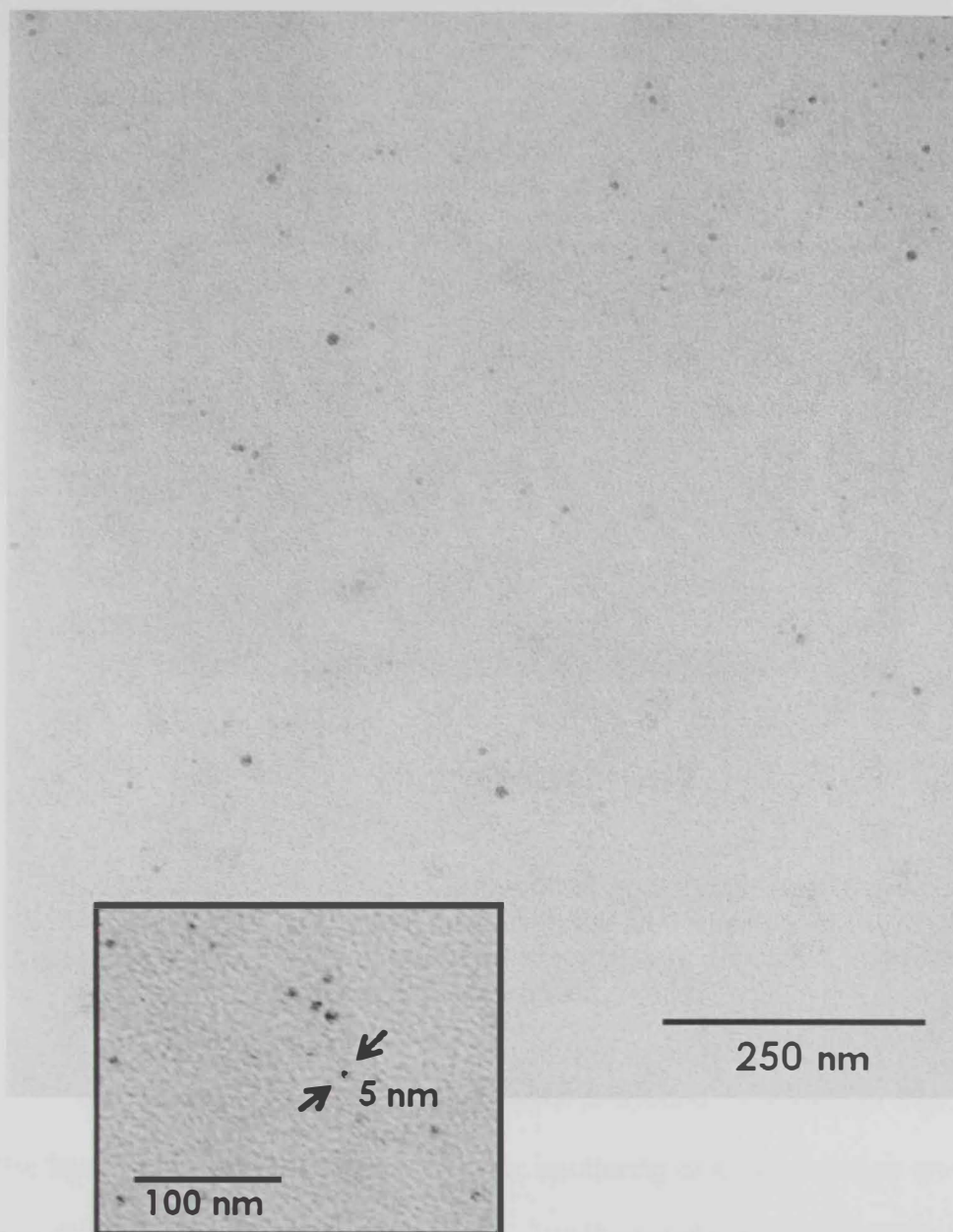
Fig. 21. A TEM image of Ag nanoclusters deposited using fAr = 60 SCCM and L = 70 mm.

Figure 22 shows a comparison of the size distribution of Ag nanoclusters synthesized with f_{Ar} = 60 SCCM and L = 70 mm measured using the QMF and the size distribution measured using the TEM images. The size distributions measured using both the TEM micrograph and QMF are in good agreement, confirming the optimum operation of the mass

filter. Figure 22 demonstrates a narrow dispersion in nanocluster size with a central value in 5.5 nm.
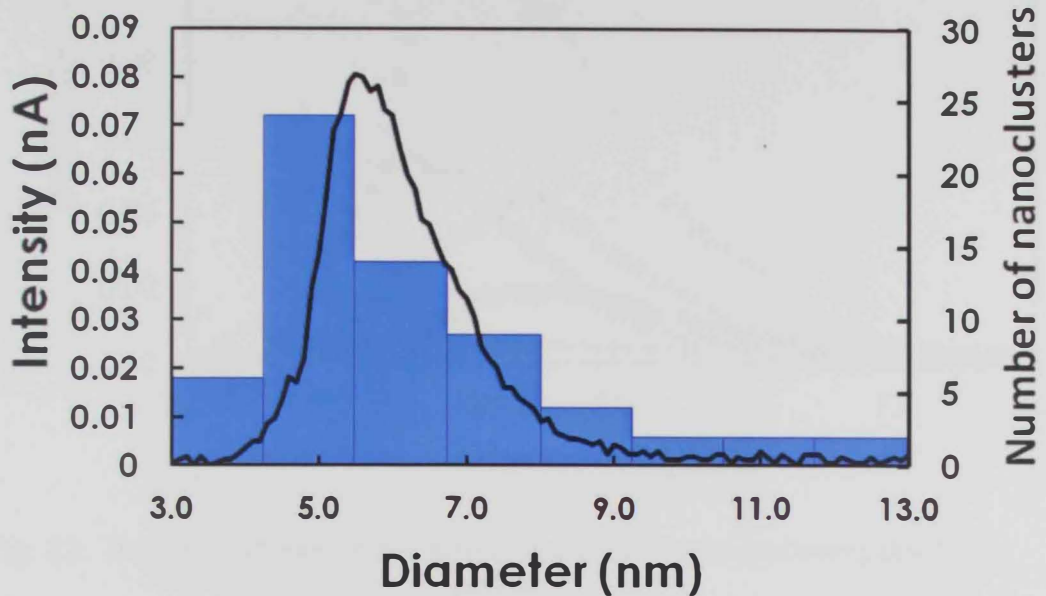
Fig. 22. Comparison of size distribution of Ag nanoclusters (fAr = 60 SCCM and L = 70 mm) measured using the QMF (solid line) with that measured using TEM (histogram) for nanoclusters deposited under the same conditions.

Nanoclusters of different sizes were produced as shown in Fig. 23. The figure illustrates the effect of the dc sputtering discharge power on the size distribution of the produced silver nanoclusters for f_{Ar} = 30 SCCM and L = 60 mm. It is observed that the produced nanoclusters exhibit a shift of the average nanocluster size distribution toward smaller sizes with increasing sputtering discharge power; and a variation of the nanocluster yield (area under curve of each size distribution), first increases with an increase in the sputtering discharge power to then decreases for higher sputtering discharge power up to 64.4 W.
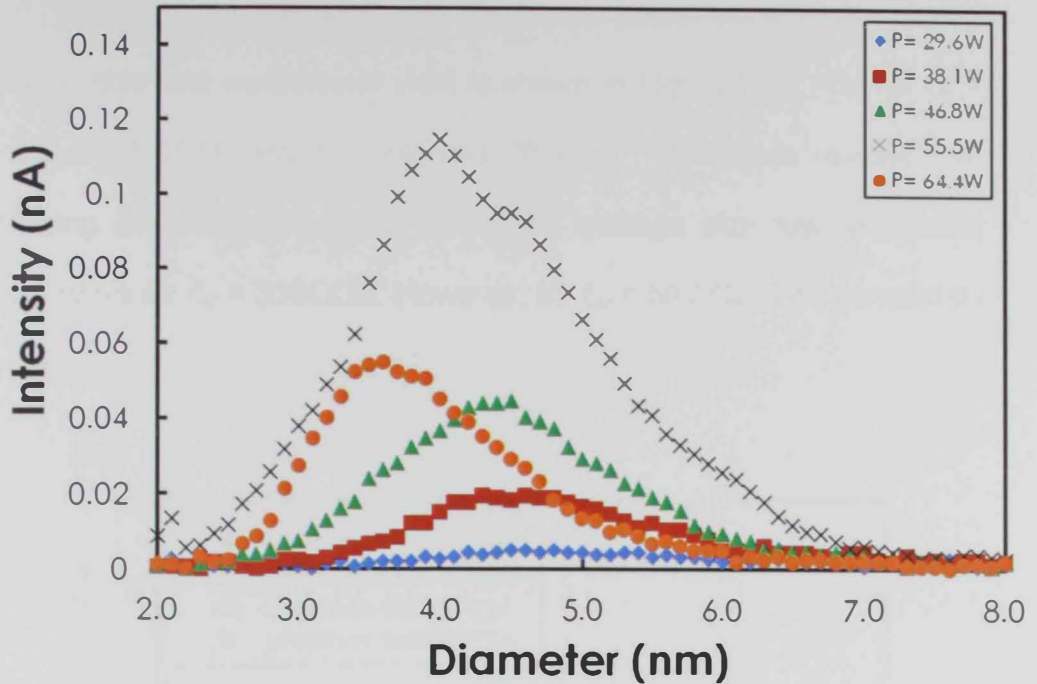
Fig. 23. The dependence of the size distribution on dc sputtering discharge power.

The dc sputtering discharge power is a major factor affecting nanocluster formation. Nanoclusters cannot be detected unless sufficient discharge power is applied to provide enough self-bias on the target as long as the plasma is stable [48, 59-60]. Increasing the discharge power usually increases the energy of Ar ions and thus the amount of ejected Ag atoms increases. However, at high discharge power the plasma becomes unstable which decrease the amount of sputtered atoms. Silver nanoclusters could be detected within a discharge power range between 29.6 to 64.4 W with stable plasma. Figure 23 illustrates that as the discharge power increases from 29.6 to 55.5 W the number of detected nanoclusters increases. Further increase in the discharge power decreases the number of detected nanoclusters.

The effect of the sputtering discharge power on the nanocluster average size and nanocluster yield is shown in Figs. 24 (a) , (b) for f_{Ar} = 30 and 50 SCCM, and L = 60 and 70 mm. The figure reveals that increasing the discharge power shifts the average size toward smaller nanoclusters for f_{Ar} = 30SCCM. However, for f_{Ar} = 50 SCCM it's completely the opposite.

(a)

(b)
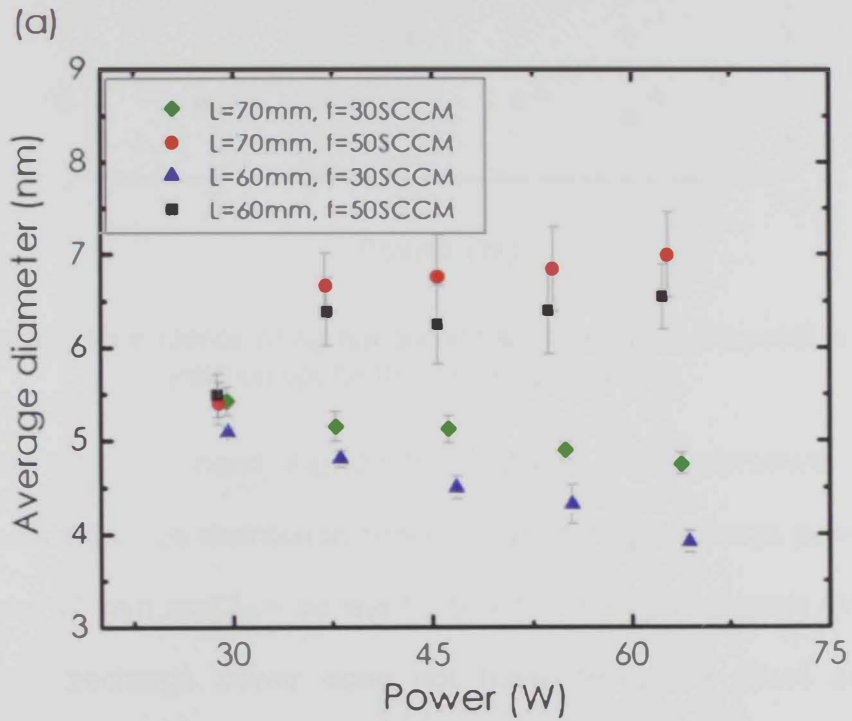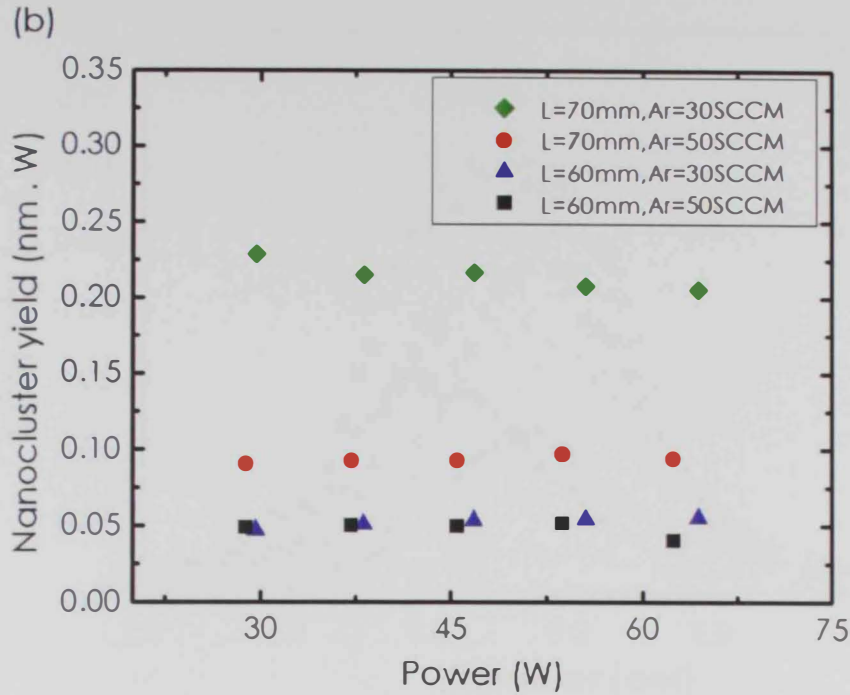
Fig. 24. The dependence of Ag nanoclusters' (a) average diameter and (b) yield on sputtering discharge power.

On the other hand, Fig. 24 (b) illustrates the dependence of the area under Ag's size distribution curves on sputtering discharge power for L= 60 and 70 mm and f_{Ar} = 30 and 50 SCCM. The figure reveals that the sputtering discharge power does not have noticeable effect on Ag nanoclusters yield for the same conditions. For L = 60 mm with different flow rates (f_{Ar} = 30, 50 SCCM) the area under the size distribution curve remains low and constant, which can be understood as: by increasing f_{Ar} more material have been sputtered, then nanoclusters will grow to large nanoclusters with maintaining the same nanoclusters yield. On the other hand, for L = 70 mm, increasing f_{Ar} will decrease the nanoclusters yield to less than the half due to the increase in the average size.
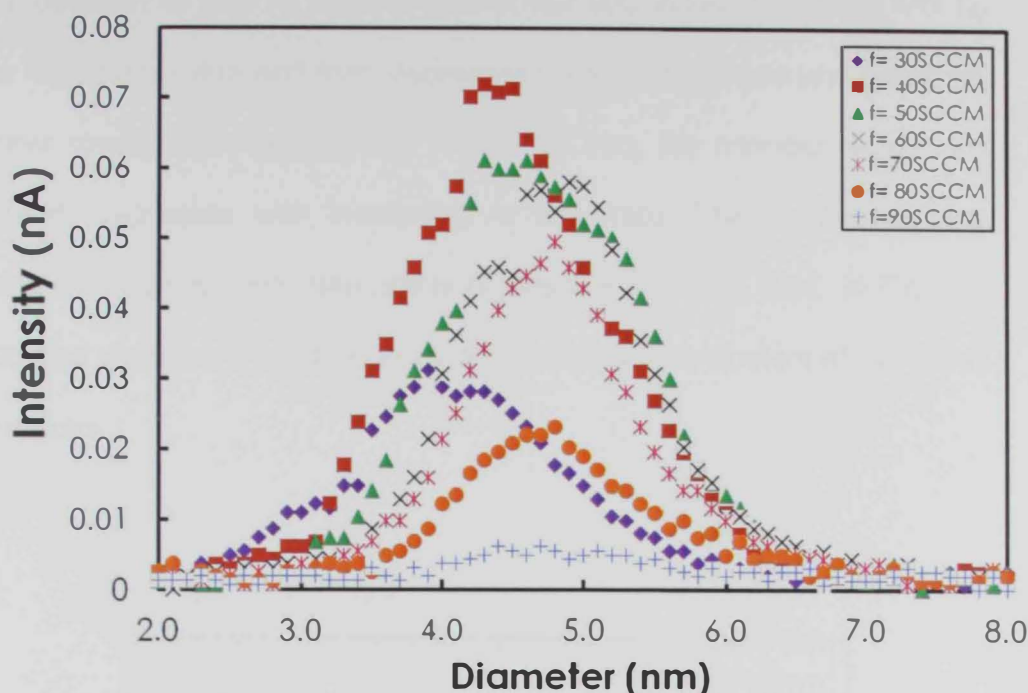
Fig. 25. The dependence of the Ag nanocluster size distribution on Ar flow rate for P = 21.5 W and L = 50 mm.

Figure 25 shows size distribution curves generated using a 21.5 W sputtering discharge power, aggregation length of 50 mm and pressure in the range of $6.2 \times 10^{-4} - 2.03 \times 10^{-3}$ mbar for different Ar flow rates. The produced nanoclusters exhibit a shift of the average nanocluster size toward larger sizes with increasing Ar flow rate, and an increase in the area under the nanocluster size distribution curves followed by a decrease. Figures 26 (a) and (b) show the dependence of silver nanoclusters' average size and yield on Ar flow rate for aggregation lengths in the range of 30 to 90 mm. The results are generated using a 21.5 W discharge power and pressure in the range of $6.2 \times 10^{-4} - 1.8 \times 10^{-3}$ mbar. The nanocluster average sizes in Fig. 26(a) were taken from size distribution curves similar to those in Fig. 25. Figure 26(a) shows that

for L between 40 and 70 mm the nanocluster size initially increases with f_{Ar} to a maximum value and then decreases before it stabilizes and becomes almost constant. However, for L = 80 – 90 mm, the nanocluster size, in general, decreases with increasing Ar flow rate. The number of size distribution curves (and data points of average size and yield in Fig. 26) produced were limited to the ability of producing nanoclusters at particular conditions.

(a)
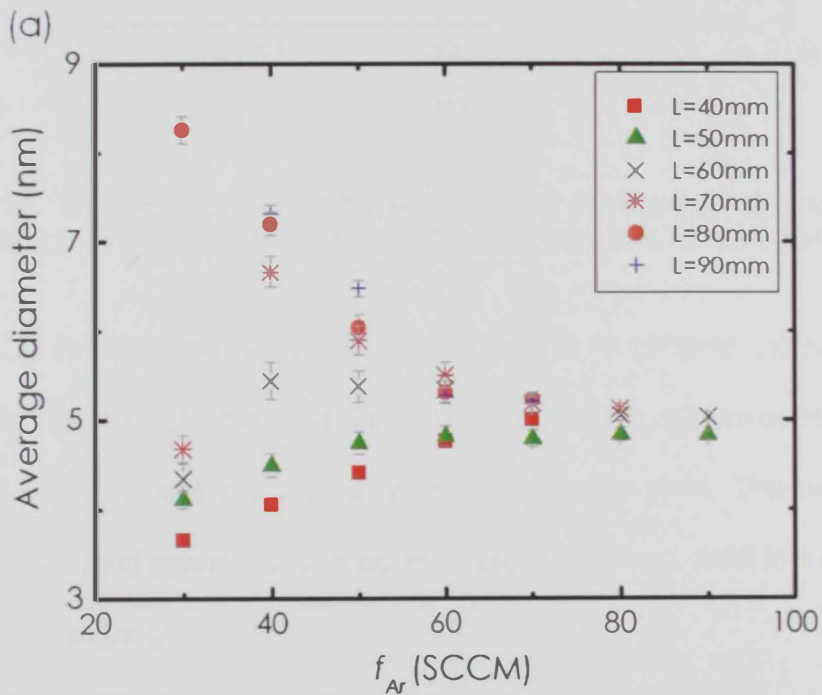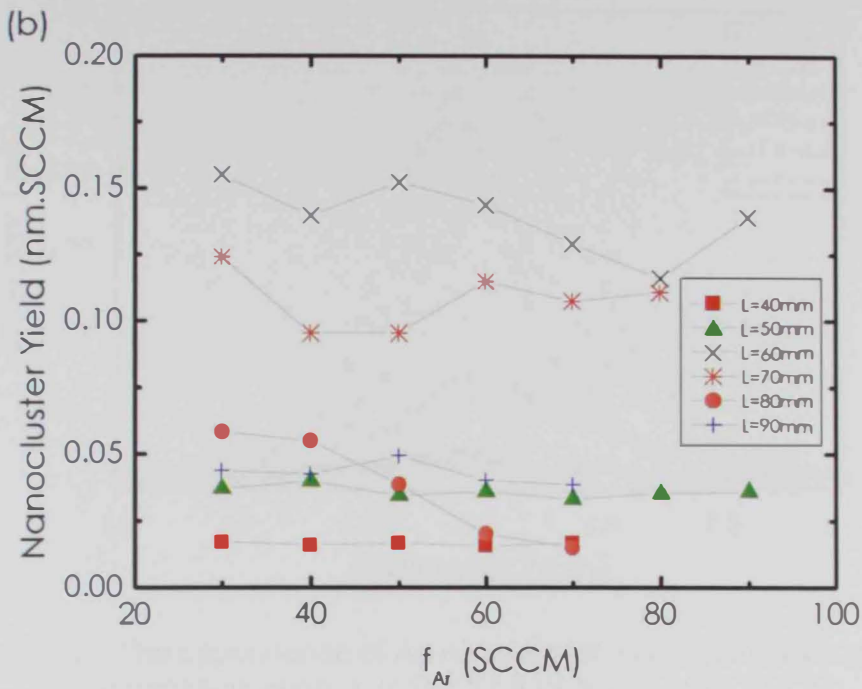
Fig. 26. The dependence of Ag nanoclusters' (a) average size and (b) yield on Ar flow rate for P = 21.5 W and L between 30 and 90mm.

On the other hand, Fig. 26 (b) shows that, in general, increasing Ar flow rate will maintain the area under size distribution curves constant (for each L) which is indicating a constant nanocluster yield. The maximum nanocluster yield occurs for L = 60 mm, and the lowest yield is for L = 40 mm (at minimum L).

Figure 27 shows size distribution curves generated using a 21.5 W sputtering discharge power, Ar flow rate of 70 SCCM and pressure of 1.56 × 10⁻³ mbar for different aggregation lengths.
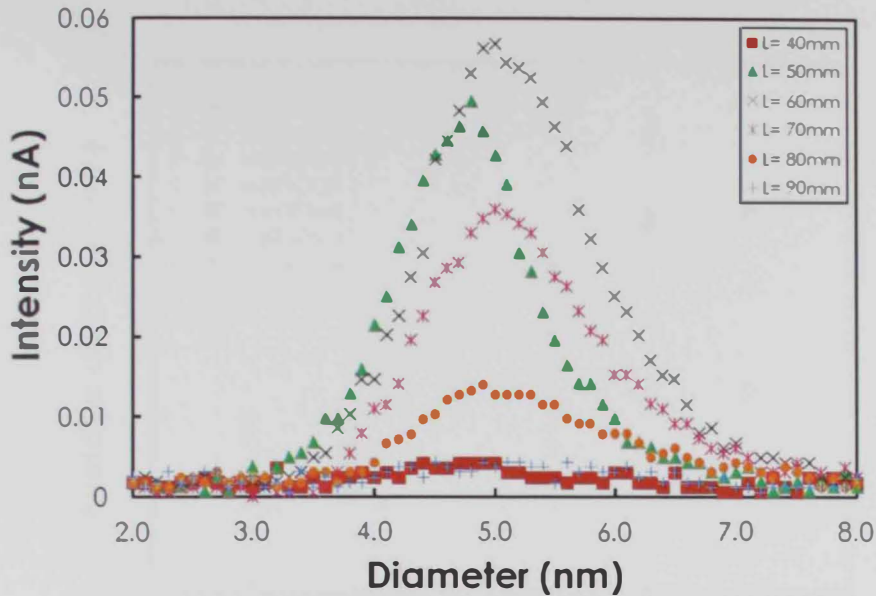
Fig. 27. The dependence of Ag nanocluster size distribution on the aggregation length L at P = 21.5 W and f_{Ar} = 70 SCCM.

The produced nanoclusters exhibit a shift of the average nanocluster size toward larger sizes with increasing the aggregation length and an increase in the nanoclusters yield with L up to 60 mm followed by a sharp decrease.

Figures 28(a) and (b) show the dependence of silver nanoclusters' average size and yield on the aggregation length for different Ar flow rates. The results are generated using a 21.5 W discharge power and pressure in the range of $6.2 \times 10^{-4} - 1.8 \times 10^{-3}$ mbar. Figure 28(a) shows that for f_{Ar} between 40 and 60 SCCM the nanocluster average size increases from 4nm to 8.5 nm. However, for f_{Ar} = 70 – 90 SCCM the nanocluster size, in general, stays constant with increasing Ar flow rate.
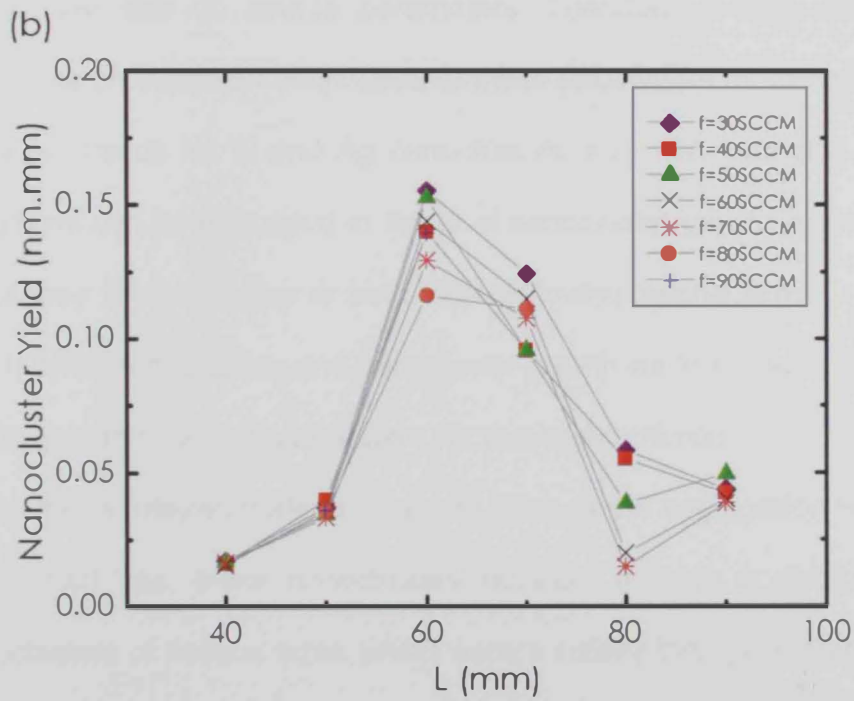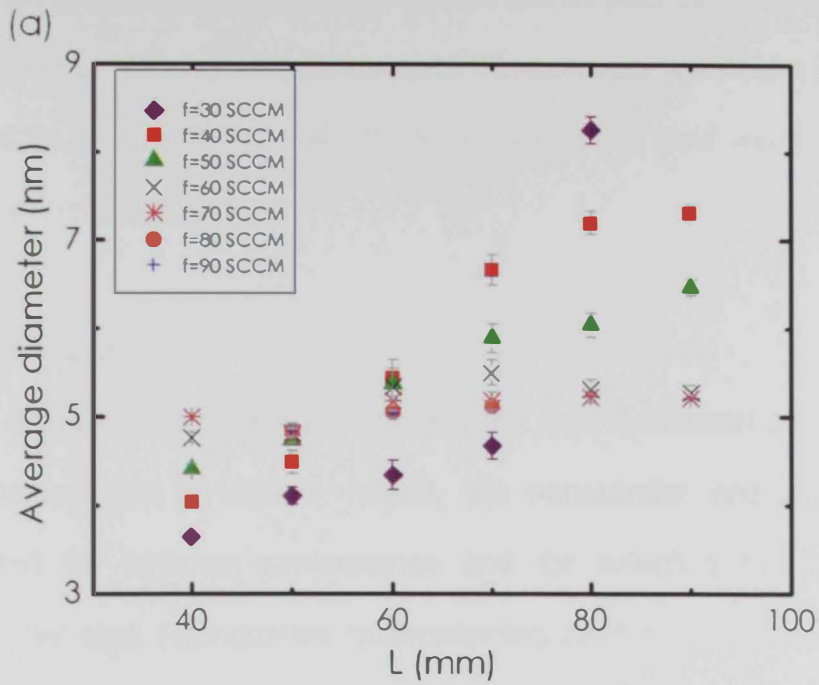
Fig. 28. The dependence of Ag nanoclusters' (a) average size and (b) yield on the aggregation length for Ar flow rates between 30 and 90 SCCM.

On the other hand, Fig. 28 (b) shows that the yield increases with L to a maximum at L = 60 mm, and then decreases. The maximum nanocluster yield was obtained for f_{Ar} = 30 SCCM, while the lowest nanocluster yield was for f_{Ar} = 70 SCCM at L = 80 mm.

4.2 Discussion

On changing the source parameters, the size distribution of produced nanoclusters can be varied, hence, the nanocluster source can be calibrated for optimum performance and for selecting the desirable nanocluster size. Furthermore, understanding the formation mechanisms of the produced nanoclusters can be realized from the dependence of the nanocluster size on source parameters. Therefore, a size distribution curve was produced for each value of these parameters for this sake. The observed trends for Si and Ag nanoclusters' size with changing source conditions can be discussed in terms of nanocluster growth phenomenon which may involves either or both of the following mechanisms:

(1) embryo nucleation and nanocluster growth via three-body collision

(2) growth to large nanoclusters via two-body collision

As the sputtered material is swept through the aggregation region by argon inert gas, these nanoclusters nucleate to form a distribution of nanoclusters of various sizes which occurs initially through the nucleation of nanocluster 'embryos' due to cooling of the sputtered atoms by Ar. The nucleation of these small embryos is followed by the growth of the embryos into larger nanoclusters. The embryo formation is initiated through three-body collision such that an Ar atom colliding with two

59

sputtered atoms and eliminating their excess kinetic energy. The nanocluster embryos are then nucleate to produce large nanoclusters via two-body collision mechanism which may take place through nanocluster growth by means of nanocluster-nanocluster collision and nanocluster growth via atomic condensation (atom-nanocluster) [60 - 61]. The nanoclusters may also grow via three-body. Consequently, the type of collision mechanism involved in nanocluster production can be used to explain the variation of the average size of the nanocluster as a function of f_{Ar} [60].

Due to the high sputter rate and great ionization, larger nanoclusters are formed as f_{Ar} increases through two-body collision mechanism. However, when f_{Ar} reach some value the nanocluster within the aggregation region will be drifted through the aggregation region more rapidly this will reduce the nanocluster nucleation and growth time, hence, two-body collision probability of the nanoclusters also decreases, and the average nanocluster size decreases [60 - 61]. The probability of the three-body collision increases as the density of the atomic vapor, and nucleation and growth time in the aggregation region increases. Therefore, when the three-body collision mechanism is dominant, as f_{Ar} increases the nucleation and growth time of the nanocluster decreases, hence, the nanocluster average size decreases due to the high drift velocity of the nanoclusters within the aggregation region [58, 60- 61]. On the other hand, when the two-body collision mechanism is dominant, as f_{Ar} increases the mean-free-path decreases, hence, the probability of the nanocluster–

nanocluster and atom-nanocluster collisions increases, and the nanocluster average size increases [55, 61].

4.2.1 Silicon results' discussion

The increase in nanocluster size with increasing f_{Ar} (Fig. 19(a)) can be assigned to the dominance of the two-body collision mechanism [34]. As f_{Ar} increases, the mean–free-path of Si atoms/clusters increases, hence, the probability of the nanocluster–nanocluster and atom-nanocluster collisions increases, and the nanocluster average size increases [60]. Furthermore, Fig. 19 (b) shows that by increasing the Ar flow rate, the nanoclusters yield decreases and reach a minimum at f_{Ar} =70 SCCM due to consuming the nanoclusters to produce larger nanoclusters. This argument is with excellent agreement with the result of Fig. 19 (a), where the increase in D with f_{Ar} is mainly due to two-body collision mechanism [35]. However, the nanocluster yield increase beyond 70 SCCM. We observed that plasma becomes less stable at high Ar flow rates, which might be related to the decrease in nanocluster yield at high f_{Ar} values.

4.2.2 Silver results' discussion

Figure 26(a) reveals that at low f_{Ar} the average size of the Ag nanoclusters increases with increasing f_{Ar} for L between 40 and 70 mm due to the small mean-free-path, where Ag nanoclusters embryos grow to produce large nanoclusters via atomic condensation and nanocluster-nanocluster collision which indicates the dominance of the two-body

61

collision mechanism [60]. On the other hand, for higher f_{Ar} the average size of Ag nanoclusters decreases with increasing f_{Ar} which can be assigned to the dominance of three-body collision mechanism. This is a direct result of reducing the nucleation and growth time in the aggregation region due to a higher drift velocity of Ag nanoclusters within the growth region. The nucleation and growth time within the aggregation region can be increased by increasing the length of the aggregation region. Figure 28(a) shows that increasing the aggregation length generally increases the average size of nanoclusters. The direct increase in the Ag nanocluster average size with L, observed in Fig. 28(a) for f_{Ar} =40 and 50 SCCM, is due to long nucleation time within the aggregation region. For Ag nanoclusters with f_{Ar} greater than 50 SCCM the initial increase in the nanocluster average size can be referred to the increase in the nucleation time. At L greater than 60 mm the nanocluster density reduces with their growth and it takes longer time for three-body collisions which atones the effect of the nucleation time. Therefore, the diameter remains approximately constant.

Nanocluster yield is given by the area under the size distribution. Figures 24(b), 26 (b) and 28(b) show the dependence of the area under each size distribution curve on: P (Fig. 24(b)), f_{Ar} (Fig. 26(b)) and L (Fig. 28(b)). It is observed that increasing Ar flow rate will maintain the area under each size distribution curve constant which is indicating a constant nanocluster yield as shown in Fig. 26(b) for each L. The small number of measured nanoclusters observed at low L could be the result of low nanocluster yield of Ag at the lowest possible L. For L between 40 and 60

mm a direct increase in the nanocluster yield was observed. The increase in the nanocluster yield with L is due to the long nucleation and growth time, which supports both nanocluster growth and yield. For L greater than 60 mm a drop in nanocluster yield is observed compared to small L values. This is a direct result of increasing L such that it will promote the nucleation and growth of nanoclusters by increasing the residence time within the aggregation region [34]. L = 60 mm has the largest measured nanocluster yield which is a result of the intermediate aggregation length which will prevent the growth to larger nanoclusters.

Figure 28(b) shows that increasing the aggregation length will increase area under each size distribution curve up to L=60 However, for f_{Ar} = 30 to 50 SCCM, the nanocluster yield decreases with increasing L as a result of increasing the average diameter which is mainly due to the dominance of the two-body collision mechanism [60]. The maximum nanocluster yield occurs for f_{Ar} = 50 SCCM. The smallest nanocluster yield was for f_{Ar} = 80 and 90 SCCM and could be the result of consuming the nanoclusters to produce larger nanoclusters which can be assigned to the dominance of three-body collision mechanism.

It was found that increasing the sputtering discharge power does not have considerable effect on Ag nanoclusters yield for L= 60 and 70 mm and f_{Ar} = 30 and 50 SCCM as shown in Fig. 24(b). The figure reveals that for L = 60 mm with different flow rates (f_{Ar} = 30 and 50 SCCM) the area under the size distribution curve remains constant. This can be assigned to the dominance of two-body collision mechanism due to the

high sputter rate and great ionization, larger nanoclusters are produced as f_{Ar} increases (i.e increasing f_{Ar} more material have been sputtered, then nanoclusters will grow to large nanoclusters while maintaining the same nanoclusters yield).

In conclusion, it has been demonstrated that IGC technique allows effective production of small nanoclusters with average size varies with the variation of source parameters, such as the length in which the nanoclusters aggregate zone (L), flow rate of inert gas (f_{Ar}), and sputtering discharge power (P). We found that f_{Ar} and L have the greatest influence on changing the nanocluster size. It was observed that the average size of Ag nanocluster initially increases with increasing Ar flow rate for small f_{Ar} due to the decrease in the mean free path which promotes the two-body collision mechanism. For large f_{Ar}, as f_{Ar} increases smaller Ag nanoclusters are produced due to reducing of the nucleation and growth time. Ag nanoclusters with diameters in the range of $3.60 - 8.26 \pm 0.15$ nm were synthesized by controlling the source conditions. It was found that as L increases, larger nanoclusters were detected as a result of the increase in the nucleation time.

CHAPTER FIVE: EFFICIENCY ENHANCEMENT OF POLYCRYSTALLINE SI SOLAR CELL USING AG NANOCLUSTERS

5.1 Introduction

As a solar cell is under illumination it absorbs incident sunlight (photons) which transfer the energy to the electrons and excite them. The solar cell can be considered as a semiconductor diode operating in the reverse bias mod e when exposed to light such that the penetration of light into the p-n junction leading to the separation of the electrons from their corresponding holes, and can thus be fed to an external circuit creating a photocurrent [62]. Figure 29 shows a simple equivalent circuit model for conventional p–n junction solar cells.
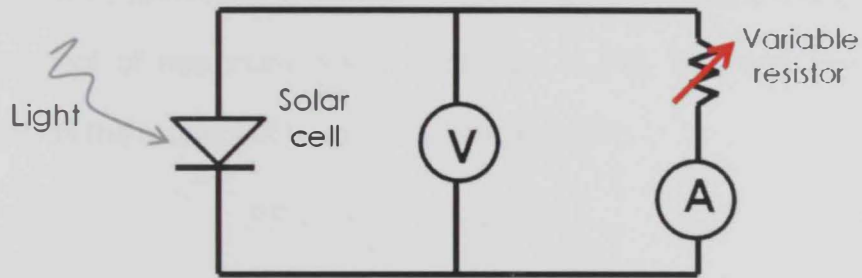
Fig. 29. A simple equivalent circuit model for conventional p–n junction solar cells [Adapted from reference [63]].

For quantifying solar cell performance, understanding and modeling of solar cell is necessary and some standard measurements must be considered [63 - 64]. Figure 30 illustrates typical I-V characteristic curve which measures the current which can be drawn out of the cell as a function of applied voltage to the cell. The results in Fig. 30 were generated in our lab for a commercial polycrystalline Si solar cell. Additionally, the rectifying behavior of the current is observed as a diode can be observed in Fig. 30 as well [11]. There are several solar cell characteristics that can be taken from the I-V characteristic curve, but the

most important characteristics describing the performance of a solar cell are:

1) Short-circuit current (I_{SC}) which represents the maximum current that may be drawn from the solar cell when the voltage across the solar cell is zero. This can be determined by the generation rate and collection probability. For a solar cell with a top area of 1 x 1 cm^2, the current measured is equivalent to the values of current density (J_{SC}) [64].

2) Open-circuit voltage (V_{OC}) which is the maximum voltage available from a solar cell when the current through the cell is zero which is a property of solar cell material.

3) Fill factor (FF) which is a parameter in the range of 0 - 1 and it is given by the quotient of maximum power (rectangle in Fig. 30), and can be determined as the product of I_{SC} and V_{OC} (circles) [65]:

$$FF = \frac{I_{max}V_{max}}{I_{sc}V_{OC}} \quad (5\text{-}1)$$

Graphically, FF is the area of the rectangle fitted by the maximum power point on the I-V curve and usually used to compare the performance of one solar cell to another.

4) Efficiency (η) which is defined as the ratio of energy output from the solar cell to input energy from the sunlight [66], and given as:

$$\eta = \frac{I_{sc}V_{OC}FF}{P_{input}} \quad (5\text{-}2)$$

Those characteristic are illustrated in Fig. 30 [64]. Therefore, to maximize the solar cell efficiency, large short circuit current and open circuit voltage should be generated, and the fill factor must be maximized as well.
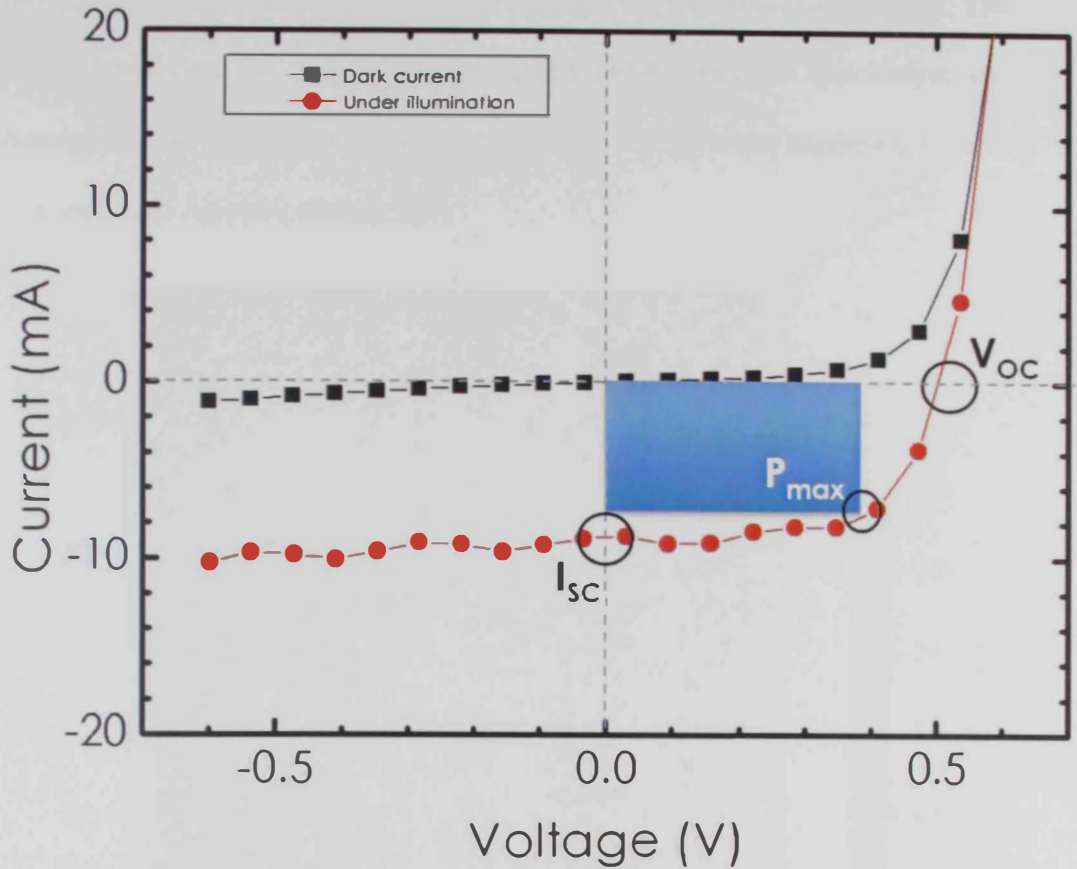
Fig. 30. I-V characteristics describing the performance of a solar cell. The results were generated in our lab for a commercial polycrystalline Si solar cell.

5.2 Experimental procedure

Commercial polycrystalline Si solar cell with an active area of 1 cm x 1cm was tested under illumination from an artificial light source with an intensity of 30 mW/cm². The I-V characteristics were measured using a Keithley 236 source measuring unit controlled by a computer. I-V measurements for the (as bought) solar cell were performed. Fill factor, I_{SC}, V_{OC} and the efficiency of the solar cell were estimated as described above. Next, 1 nm thick Ag nanocluster film was deposited on top of the same solar cell. Ag nanoclusters were fabricated as discussed above with f_{Ar} = 50 SCCM, L = 70 mm and P = 46.8 W. The average nanocluster size

was 6.75 nm. Figure 31 shows an AFM image of the deposited nanoclusters. The image shows that the deposited nanoclusters exhibit random distribution and coverage of less than a monolayer. I-V measurements were repeated for the solar cell with Ag nanocluster film.
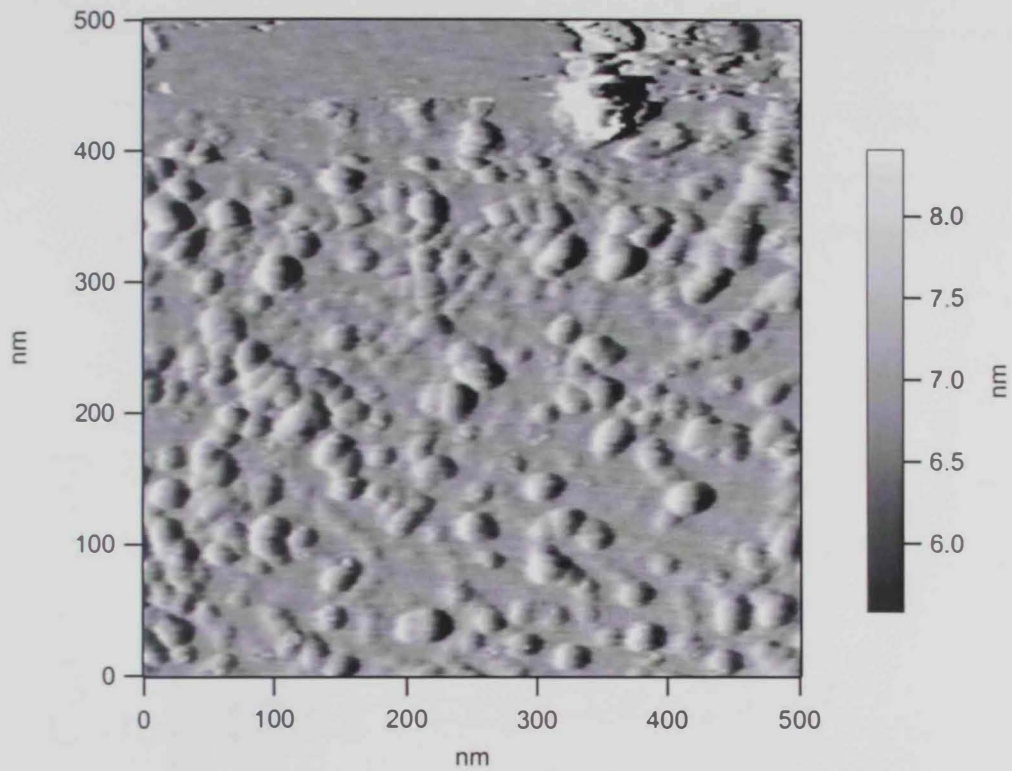
Figure 31: AFM image of the Ag nanoclusters deposited on a commercial Si solar cell using f_{Ar} = 50 SCCM, L = 70 mm and P = 46.8 W.

5.3 Results

The electrical characteristics of polycrystalline Si solar cell before and after the deposition of Ag nanoclusters in dark and under illumination are summarized in Table 1 and Fig. 32.

Table 1. Electrical characteristics of polycrystalline Si solar cell before and after the deposition of Ag nanoclusters.

	Before deposition of Ag nanoclusters	After deposition of Ag nanoclusters
J_{SC} (mA/cm^2)	7.774	8.904
V_{OC} (V)	0.487	0.503
FF	63.1%	65.4%
η	7.96%	9.76%

Fig. 32. I-V characteristic of crystalline Si solar cell in dark, and under illumination before and after deposition of 1nm thick Ag nanocluster film.

A 14.5 % increase in the short-circuit current is observed. The short-circuit current results of the generation and collection of light-generated carriers. Additionally, 3.28 % increase in the open-circuit voltage (V_{OC}) is detected. Therefore, a 22.7 % increase in the solar cell

efficiency enhancement can be calculated after deposition of Ag nanoclusters.

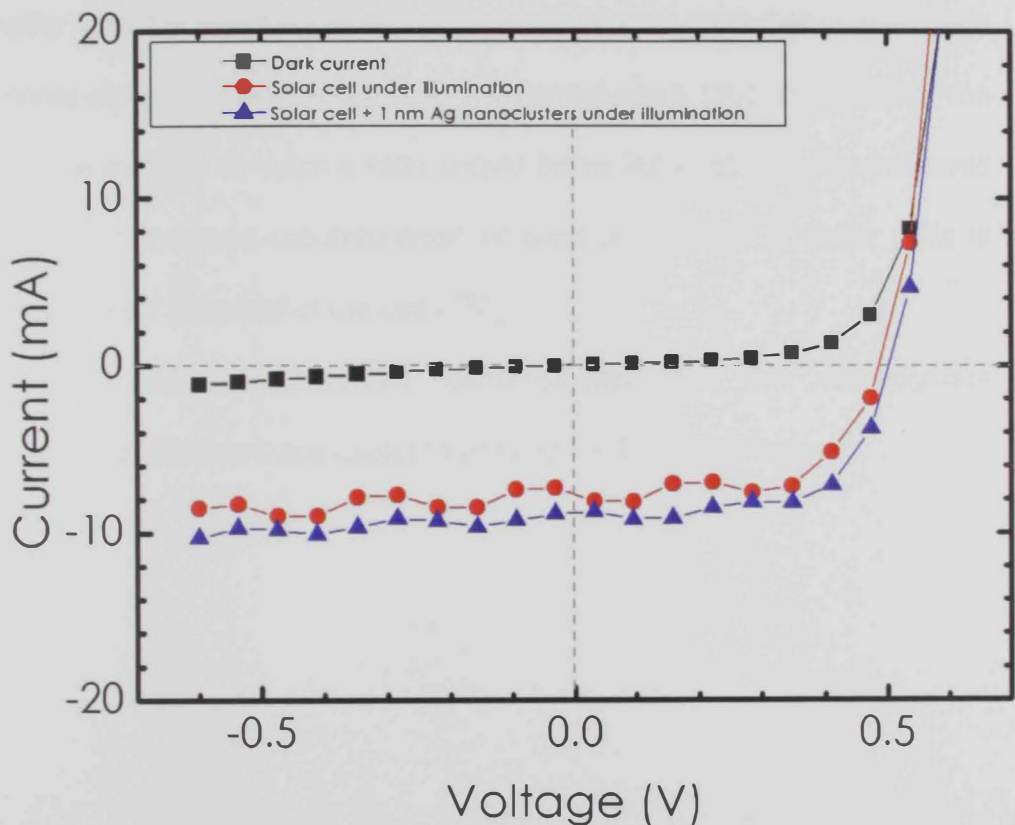The enhancement in solar cell efficiency is attributed to the improvement of light absorption in solar cell due to enhancement of light trapping because of the Ag nanoclusters on the solar cell surface [30]. Herein, Scattering and absorption of light depend on the size of nanoclusters on solar cell's surface. Ag nanoclusters that are much smaller than the wavelength of light tends to absorb more hence extinction is dominated by absorption in the Ag nanoclusters [30]. In addition, the immense surface to volume ratio provid better light-trapping mechanisms that do not increase recombination of electron-hole los in solar cells to extract the full potential of the cells [30].

The above experiment demonstrates that the nanoclusters generated in this work are useful to enhance solar cell efficiency.

CHAPTER SIX: CONCLUSION AND FUTURE DIRECTIONS

6.1 Conclusion

This thesis has been concerned with the study of the syntheses of silicon (Si) and silver (Ag) nanoclusters by means of inert gas condensation and dc magnetron sputtering. The main reason for focusing on silicon and silver nanoclusters is the possibility of using them for solar cell applications. It has been demonstrated that this technique allows effective production of small and narrow size range of nanoclusters with average size varies with the variation of different parameters, such as the length in which the nanoclusters aggregate (L), the flow rate of inert gas (f_{Ar}) (in our case argon inert gas was used), and the sputtering discharge power (P). Si nanoclusters were produced with mean size in the range of 3.33 ± 0.27 nm to 7.36 ± 0.52 nm by controlling the source conditions as witnessed by TEM images. A quadrupole mass filter was used to filter and study the nanocluster size distribution. We found that f_{Ar} and L have the greatest influence on changing the nanocluster size. In general, f_{Ar} has the greatest effect on Si nanoclusters average size. On the other hand, it was observed that the average size of Ag nanocluster initially increases with increasing Ar flow rate for small aggregation lengths due to the small mean free path such that nanoclusters embryos grow to produce large nanoclusters via two-body collision mechanism. For larger f_{Ar}, as f_{Ar} increased smaller Ag nanoclusters were produced due to the reducing of the nucleation and growth time (the time spent by nanoclusters within the aggregation region) via three-body collision mechanism. Ag nanoclusters

71

with diameters of 3.65 ± 0.05nm to 8.25 ± 0.15 nm were synthesized by controlling the source conditions. In addition, it was found that as L increases, larger nanoclusters were detected as a result of the increase in the nucleation time. SEM was used to confirm the presence of Ag nanoclusters and their average size. TEM images were used to evaluate sizes of silicon and silver nanoclusters produced, and to confirm the reliability of the quadrupole mass filter. This work illustrates production of Si and Ag nanoclusters by a physical method, and the ability of controlling their size by proper optimization of the operation conditions.

Ag nanoclusters were deposited on commercial polycrystalline solar cells and the I–V characteristics (short circuit current, open circuit voltage, fill factor, and efficiency) were examined under light source with an intensity of 30 mW/cm^2. A 22.7% increase in the solar cell efficiency enhancement could be calculated after deposition of Ag nanoclusters which demonstrates that the nanoclusters generated in this work are useful to enhance solar cell efficiency.

6.2 Future Directions

Tunability of nanocluster size distribution is a very important factor in the development of solar cell and optoelectronic devices. The synthesis of silicon and silver nanoclusters is still an ongoing research field. Using the inert gas condensation technique to synthesis nanoclusters provides inspired growing research interest because of its variability and flexibility in materials synthesis. Also, due to the wide available nanoclusters size range. Inert gas flow rate, aggregation length, and sputtering discharge

72

power play crucial roles in predicting the nanocluster size. Obtaining a better understanding of the effect of these parameters on nanocluster size would further improve the mathematical models, thus enabling better control on nanocluster size. There are also many future directions which can be applied in the near future, especially, production of the field of nanocluster materials is a hot new research area. The following is a brief list of directions in which researchers can peruse:

1- Studying the effects of temperature on nanocluster size as well as the morphology and size distributions.

2- Fabricating solar cells using the produced Si and Ag nanoclusters with different sizes using this research results.

3- Studying the enhancement of the Ag surface plasmon on solar cells.

4- Studying the effect of the nanocluster shape on enhancing the efficiency of the solar cells.

Ultimately, the results produced and the knowledge gained has enhanced our understanding of the production of nano-scale materials. The obtained data will improve current state of the art knowledge of the behavior of silicon and silver nanoclusters. The results and discussions made in this study will help answering essential questions about controlling of Si and Ag nanoclusters size.

REFERENCES

[1] N. Taniguchi, Proc. Intl. Conf. Prod. Eng. **2**, 18 (1974).

[2] M. Ashby, P. Ferreira and D. Schodek. Nanomaterials, Nanotechnologies and Design, Elsevier Ltd (2009).

[3] R. Meyer, J.J. Gafner, S.L. Gafner, S. Stappert, B. Rellinghaus, P. Entel, Phase Trans. **78**, 35 (2005)

[4] Nanoscience and nanotechnologies: opportunities and uncertainties, The Royal Society,July, 2004.

[5] S. W. Tong, C. F. Zhang, C. Y. Jiang, G. Liu, Q. D. Ling, E. T. Kan, Chem. Phy. Lett. **453**, 73 (2008).

[6] A.I. Maaroof, G.B. Smith,Thin Solid Films **485**, 198 (2005).

[7] P. Hervés, M. Pérez-Lorenzo, L. M. Liz-Marza'n , Joachim Dzubiella, Y. Lu and M. Ballauff, Chem. Soc. Rev. **41**, 5577 (2012).

[8] M. Arruebo, R. F. Pacheco, M. R. Ibarra, and J. Santamaria, Nano Today **2**, 22 (2007).

[9] Haley B. and Frenkel E., Urol. Oncol. Semin. Orig. Invest. **26** (1), 57(2008).

[10] B. Kateb, K. Chiu, K. L. Black, et al., NeuroImage **54**, S106 (2011).

[11]Thomas L. Floyd: Electric Devices Conventional Current Version(Pearson, United States of America, 2005)

[12] G. Jaeckel, Z. Tech. Phys. **6**, 301(1926).

[13] P. Harrison, Quantum wells, wires and dots, Wiley, 2005.

[14] R. Carbone, I. Marangi, A. Zanardi, et al., Biomaterials **27**, 3221(2006)

[15] J. A. Collines, C, Xirouchaki, J. K. Heath, C. H. Jones, App. Surf. Sci. **226**, 197 (2004).

[16] V. Straňák,S. Block, S. Drache, Z. Hubička, C. A. Helm, L. Jastrabík, M.Tichý and R. Hippler, Surf. Coat. Technol. **205**, 2755 (2011).

[17] W.A. de Heer, Rev. Mod. Phys. **65**, 611 (1993)

[18] M. Stupca, M. Alsalhi, T. Al Saud, and A. Almuhanna, and M. H. Nayfeh, Appl. Phys. Lett. **91**, 063107 (2007).

[19] Y. Matsumoto, G. Hirata, H. Takakura, H. Okamoto, and Y. Hamakawa, J. Appl. Phys. **67**, 6538 (1990).

[20] J. Szlufcik , S. Sivoththaman, J.F.Nlis, R. P. Mertens, and R. J.Van Overstraeten, Proc. IEEE **85**, 711 (1997).

[21] C. Meier, A. Gondorf, S. Luttjohann, and A. Lorke, J. Appl. Phys. **101**, 103112 (2007).

[22] F. J. Beck, A. Polman, and K. R. Catchpole, J. Appl. Phys. **105**, 114310 (2009).

[23] D. B. Sanchez, PhD thesis, Madrid University (2007).

[24] X. Huang, M. A. El-Sayed, J. Adv. Res.**1**, 13 (2010).

[25] K. L. Kelly, E. Coronado, L. L. Zhao, G. C. Schatz, J. Phys. Chem. B **107**, 668 (2003).

[26] D. Duche, P. Torchio, L. Escoubas, F. Monestier, J. Simon, F. Flory and G. Mathian, Sol. Energy Mater. Sol. Cells **93**, 1377 (2009).

[27] S. K. Ghosh and T. Pal, Chem. Rev. **107**, 4797 (2007).

[28] C. F. Bohren and D. R. Huffman, Absorption and Scattering of Light by Small Particles, Wiley-Interscience, New York, 1983.

[29] C. F. Bohren, Am. J. Phys. **51**, 323 (1983).

[30] S. Pillai, K. R. Catchpole, T. Trupke, and M. A. Green, J. Appl. Phys. **101**, 093105 (2007).

[31] E. T. Yu, D. Derkacs, S. H. Lim, P. Matheu, and D. M. Schaadtc, Proc. of SPIE **7033,** 70331V (2008).

[32] K. Lee, S. Lin, C. Lin, C. Tsai and Y. Lu, Surf. Coat. Technol. **202**, 5339 (2008).

[33] M. A. Green, K. Emery, Y. Hishikawa, W. Warta, E.D. Dunlop, Prog. Photovoltaics Res. Appl. **20**, 12 (2011).

[34] A. I. Ayesh, N. Qamhieh, H. Ghmlouche, S. Thaker, and M. El-shaer. J. App. Phys. **107**, 034317 (2010).

[35] A. N. Banerjee, R. Krishna, and B. Das, Appl. Phys. A: Mater. Sci. Process. **90**, 299 (2008).

[36] A.T. Fiory, and N.M. Ravindra, J. Electron. Mater. **32**, 1043 (2003).

[37]G. Spencer, B. Anyamesem-Mensah, H. C. Galloway, A. Bandyopadhyay, and D. Frasier, J. Vac. Sci. Technol. A **29**, 051508 (2011).

[38] F. Huisken, H. Hofmeister, B. Kohn, M.A. Laguna, and V. Paillard, Appl. Surf. Sci. **154–155**, 305 (2000).

[39] S. Iwasita, T. Inoue, K. Koga, M. Shiratani, S. Nunomura, and M. Kondo, IEEE Conf. Pub. **2**, 1664 (2006).

[40] A. Pyatenko, K. Shimokawa, M. Yamaguchi, O. Nishimura, M. Suzuki, Appl. Phys. A **79**, 803 (2004)

[41] Martijn H. R. Lankhorst, Bas W. S. M. M. Ketelaars and R. A. M. Wolters, Nat. Mater. **4**, 347 (2005).

[42] B. P. Rand, P. Peumans, and S. R. Forrest, J. Appl. Phys. **96**, 7519 (2004).

[43] L. Sirbu, V. Sergentu, V. Ursaki, I. Tiginyanu , G. Piredda and R. W. Boyd, IEEE Conf. Pub. **1**, 116 (2008).

[44] S. K. Srivastava, D. Kumar, Vandana, M. Sharma, R. Kumar and P. K. Singh, Sol. Energy Mater. Sol. Cells **100**, 33 (2012).

[45] C. G. Granqvist and R. A. Buhrman, J. Appl. Phys. **47**, 2200 (1976).

[46] H Hahn and RS Averback; J. Appl. Phys. **67**, 1113 (1990).

[47] A. K. Ali, D. N. Raouf, Eng. & Tech. Journal **29**, 3058 (2011).

[48] M. Ohring: Materials Science of Thin Films, 2nd ed. (Academic Press, San Diego, CA, 2002).

[49] N. H. Haia, R. Lemoinea, S. Remboldta, M. Stranda,d, J. E. Shieldb, D. Schmitterb, R. H. Kraus, Jr. M. Espyc, D. L. Leslie-Pelecky, J. Magn. Magn. Mater. **293**, 75 (2005).

[50] R. Chandra, P. Taneja, J. John and P. Ayyub, NanoStruc. Mat. **11**, 8, 1171, (1999).

[51] M. Raffia, A.K. Rumaiza, M.M. Hasan and S. I. Shaha, J. Mater. Res. **22**, 3378 (2007).

[52] E. Pérez-Tijerina, M. G. Pinilla, S. Meji'a-Rosales, U. Ortiz-Méndez, A. Torres, M. José-Yacama'n, Faraday Discuss **138**, 353 (2008).

 [53] M. Á. Gracia-Pinilla, D. Ferrer, S. Mejía-Rosales, E. Pérez-Tijerina , Nanoscale Res Lett **4**, 896 (2009).

[54] W. Knauer, J. Appl. Phys. **62**, 841 (1987).

[55] T. Hihara and K. Sumiyama, J. Appl. Phys. **84**, 5270 (1998).

[55] Nanogen-50 User Manual (Mantis Deposition Ltd., Oxfordshire, 2009).

[57] Sputtering Sensor (INFICON, 2009).

[58] P. H. Dawson, Quadrupole Mass Spectrometry and its Applications

(Elsevier, Amsterdam, 1976); Pfeiffer Quadrupole Mass Filter User Manual (Pfeiffer Vacuum GmbH, Germany, 2009).

[59] S. Pratontep, S.J. Carroll, C. Xirouchaki, M. Streun, and R.E. Palmer, Rev. Sci. Instrum. **76**, 045103 (2005).

[60] A. I. Ayesh, N. Qamhieh, and S. T. Mahmoud, J. Mater. Res., **27**, 18, 2441 (2012).

[61] M. Á. Gracia-Pinilla, E. Martý´nez, G. S. Vidaurri, and E. Pérez-Tijerina, Nanoscale Res. Lett. **5**,180 (2010).

[62] G.R. Walker, Journal of Electrical & Electronics Engineering **21**, 49 (2001).

[63] J. Yuncong, J.A.A. Qahouq, and I. Batarseh, 2010 IEEE International Symposium on Circuits and Systems, 2770 (2010).

[64] K. Tvrdy and P.V. Kamat, Comprehensive Nanoscience and Technology **4**, 257 (2011).

[65] A. K. Das, Solar Energy **85**, 1906(2011).

[66] A.S. Obaid, Z. Hassan , M.A. Mahdi, and M. Bououdina, Solar Energy **89**,143 (2013).

إنتاج جسيمات نانوية لأغراض استخدامها في تطبيقات الخلايا الشمسية

إعداد

هيله محمد الدوسري

ماجستير علوم وهندسة المواد

كلية الهندسة

جامعة الإمارات العربية المتحدة

رسالة مقدمة لاستكمال متطلبات الحصول على درجة الماجستير في علوم وهندسة المواد

جامعة الإمارات العربية المتحدة

بإشراف الدكتور أحمد عايش

إبريل 2013